UNIWERSYTET JAGIELLOŃSKI
INSTYTUT FIZYKI

# Badanie rozpadu mezonu $\eta$ na $\pi^+\pi^-e^+e^-$ za pomocą detektora WASA–at–COSY.

Michał Janusz

Praca wykonana pod kierunkiem
dra hab. Pawła Moskala, prof. UJ

Kraków 2010

# JAGELLONIAN UNIVERSITY
# INSTITUTE OF PHYSICS

# Study of the $\eta$ meson decay into $\pi^+\pi^-e^+e^-$ using WASA–at–COSY detector system.

Michał Janusz

The thesis is supervised by:
prof. Paweł Moskal
Jagellonian University
Cracow, Poland

Cracow 2010

# Contents

# Chapter 1

# Introduction

The $\eta$ meson is the eigenstate of the Parity (P), Charge conjugation (C) and combined (CP) operators. It is a rare feature in the particle physics field therefore the studies of the $\eta$ meson decays constitute a valuable source of information about the level of C, P and CP conservation. The CP violation effect was discovered in 1964 by James Cronin and Val Fitch in the decays of long lived neutral kaons ($K_L$) into two pions. Processes which violate CP symmetry have been also observed in $K_L$ leptonic decays by the KTeV [1] and NA48 [2] collaborations and in B mesons decays by Belle [3] and BaBar [4] experiments. Recently a CP violation larger than 14 % [2] has been observed in flavor-changing weak decays of neutral kaons $K_L \to \pi^+\pi^-\gamma^* \to \pi^+\pi^-e^+e^-$ and also significant violation in decays of B mesons ($B \to \pi^+\pi^-\gamma^*$) [5, 6, 7]. However, so far there is no experimental indications for the violation of CP symmetry in flavor-conserving reactions. The $\eta \to \pi^+\pi^-e^+e^-$ decay gives the possibility to study the degree of CP symmetry conservation in such reaction via the distribution of angle between pions and electrons emission planes. In this case the CP symmetry violation would manifest itself as an asymmetry of around the 90°. However a flavor conserving CP violation is not predicted in the framework of Standard Model. Therefore, the signal of such asymmetry could be a discovery of a process beyond nowadays understanding of the world of particle physics. It should be emphasized that the level of the proposed flavor–conserving CP violation effect in $\eta \to \pi^+\pi^-e^+e^-$ is not restricted via upper limit for the level of the neutron dipole moment. A possible source of the CP violation in the $\eta \to \pi^+\pi^-e^+e^-$ decay could be an interference between electric and magnetic amplitudes responsible for significant linear polarization of the photon in the $\eta \to \gamma^\star\pi^+\pi^-$. The polarization can be studied as the asymmetry in the distribution of the angle between $e^+e^-$ and $\pi^+\pi^-$ emission planes. Asymmetry up to 1% is not excluded by the other experiments [8, 9]. In order to reach an accuracy better than 1 percent in the determination of the asymmetry a sample of few tens of thousands of $\eta \rightarrow \pi^+\pi^-e^+e^-$ events is required.

The decay has been observed by CMD–2 collaboration [10]. In the year 2007 when this work was commenced there was also one measurement of the $\eta \rightarrow \pi^+\pi^-e^+e^-$ decay reported by the CELSIUS/WASA collaboration where the $\eta$ mesons was produced in proton-deuteron collision via $pd \rightarrow ^3He\eta$ reaction at threshold. In the analysis 12 candidate events were identified and the branching ratio of $(4.4 \pm 1.4) \cdot 10^{-4}$ for the $\eta \rightarrow \pi^+\pi^-e^+e^-$ channel was extracted [8]. Due to lack of statistics a detailed analysis was not possible.

The aim of this work was to make a next step on the way to the asymmetry determination and to increase the statistics using the WASA–at–COSY facility. The WASA detector has been successfully transferred from The Svedberg Laboratory in Uppsala, Sweden to the Research Centre Jülich in Germany. After initial test the first production run has been carried out in April 2007 using a proton beam with kinetic energy of 1400 MeV and a hydrogen pellet target. The next measurement with the deuteron target was performed in November 2008 and this experiment constitutes the experimental basis for this thesis. The $\eta$ meson has been produced via $pd \rightarrow ^3He\eta$ reaction using the COSY proton beam and the deuteron pellet target of the WASA detector. The kinetic energy of $^3He$ was determined based on its energy loss in the scintillators planes placed in the forward part of the WASA–at–COSY detector facility. The momentum direction of $^3He$ has been determined from direction of its trajectory reconstructed using signals in drift chambers built out of gaseous straws proportional counters. The identification of the $\eta$ mesons has been realized using conservation of the energy and momentum via calculation of the missing mass. The decay products have been measured in the central part of the WASA–at–COSY detector which covers 96 percent of the full solid angle. Four momentum vectors of the leptons and $\pi^+$ and $\pi^-$ have been determined using the track curvature reconstructed from signals in seventeen cylindrical planes of mylar straw detectors. The straw chamber has been placed inside the Superconducting Solenoid delivering magnetic field parallel to the COSY ion beam. The identification of pions and leptons is done by the energy loss in a plastic scintillator barrel and an electromagnetic calorimeter surrounding the straw chamber.

The aim of this thesis is to increase by at least an order of magnitude the sample of $\eta \rightarrow \pi^+\pi^-e^+e^-$ events with respect to the statics available from previous measurement [11], to determine the branching ratio for this channel and hence to make a proof of principle for the long–term program at WASA–at–

COSY detector to establish the asymmetry in the angular distribution of the $\pi^+\pi^-$ and $e^+e^-$ planes from the $\eta \to \pi^+\pi^-e^+e^-$ decays with the precision better than 1%.

Chapter 3 describes the detector setup of the WASA–at–COSY experiment. We focus on components which were crucial for the registration of $\eta$ charged decay modes. In addition more detailed in Chapter 4 the functioning and calibration methods of proportional gaseous detector have been discussed in example of the Forward Proportional Chamber (FPC) since the author of this thesis was responsible for its test, installation and operation.

Chapter 5 underlines the analysis chain starting from the basic selection criteria for the $^3He$ and $\pi^+\pi^-e^+e^-$ final state. Further, more detailed studies are presented for Monte Carlo simulation of possible background channels originating from other $\eta$ meson decay modes as well as direct production of pions in proton–deuteron scattering. This chapter comprises also the description of the background suppression and the estimation of the branching ratio of the $\eta \to \pi^+\pi^-e^+e^-$ decay, along with determination of the angular asymmetry between the $\pi^+\pi^-$ and $e^+e^-$ emission planes as well as appraisal of the statistical and systematical uncertainties. Finally, the work is concluded with summary and outlook.

## Chapter 2

# Theoretical background and physics motivation

### 2.1 The $\eta$ meson

Eta is a pseudoscalar meson with quantum numbers: $I^G(J^{PC}) = 0^+(0^{-+})$, where G denotes G – parity, I –isospin, J – spin, P – parity, and C charge conjugation. The $\eta$ meson is an eigenstate of the CP operator with the eigenvalue equal to -1. For further details the interested reader is referred to publication [12].

### 2.2 Decay amplitude of the $\eta \to \pi^+\pi^-e^+e^-$

In general decay amplitude is described by combination of four momentum vectors of the involved particles [13]. The $\eta \to \pi^+\pi^-e^+e^-$ decay can proceed via $\eta \to \pi^+\pi^-\gamma^*$ state where subsequently the intermediate virtual[1] photon $\gamma^*$ converts to $e^+e^-$ pair. The state of $\gamma$ quantum can be described by parity and angular momentum. Photon of total angular momentum $j$ and parity $(-1)^j$ is referred to as electric $2j$–pole, and a photon with a total angular momentum j and parity $(-1)^{j+1}$ is called magnetic $2j$–pole.

The photon eigenvalue for the charge conjugation operator is C = -1. Thus, magnetic and electric dipole states posses P,C and CP eigenvalues as given in the below table:

| **photon** | **angular momentum** | **P** | **C** | **CP** |
|---|---|---|---|---|
| E–electric | 1 | -1 | -1 | +1 |
| M–magnetic | 1 | +1 | -1 | -1 |

---

[1] It has the same quantum numbers as a real photon, except that its mass is not equal to zero.

In principle the decay amplitude can be described by magnetic and electric terms of the direct emission and internal bremstrahlung processes shown in Fig 2.1.

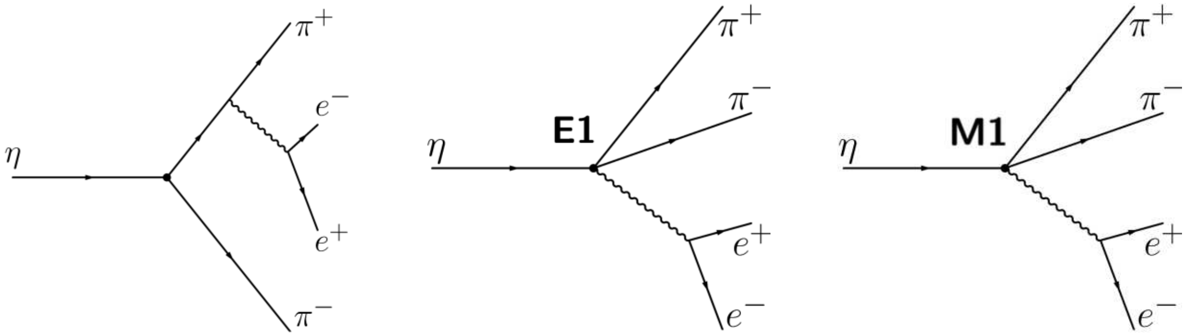

Figure 2.1: Possible contributions to the decay amplitude of $\eta \rightarrow \pi^+\pi^-e^+e^-$: left – internal bremsstrahlung radiation, center – direct emission of E1 type (electric type), right – direct emission of M1(magnetic type) type.

The decay amplitude may be then decomposed as follows:

$$A\left(\eta \rightarrow \pi^+\pi^-e^+e^-\right) = M_B + M + E \tag{2.1}$$

where $M_B$ denotes the amplitude responsible for internal bremsstrahlung radiation from one of the pions which is forbidden due to the underlying CP violating $\eta \rightarrow \pi^+\pi^-$ decay mode, and M and E stands for the direct emission process. A particular amplitudes are connected with the following CP values:

- $M_B$ CP–violating bremsstrahlung radiation with CP =+1.
- $E$ CP–violating direct emission of electric photon with CP =+1.
- $M$ CP–conserving direct emission of magnetic photon with CP =-1.

The differential decay rate of the $\eta \rightarrow \pi^+\pi^-\gamma^*$ can be formulated as it has been done in the kaons case [14]:

$$\frac{d\Gamma}{d\phi} = A\sin^2\phi + B\cos^2\phi + C\sin 2\phi \tag{2.2}$$

where $\phi$ is dihederal angle between $\pi^+$ and $\pi^-$ plane and polarization vector of the virtual photon. It is important to note that the first and the second term is symmetric in $\phi$ around 90° whereas the third term is antisymmetric. Coefficient A is due to bremsstrahlung amplitude $M_B$, B due to the direct emission amplitude, whereas C describes the interference of the two amplitudes.

## 2.3 Manifestation of the CP violation in the $\eta \rightarrow \pi^+\pi^-e^+e^-$ decay

The mechanism leading to the large CP–violation can be explained by the interference between the CP–violating and CP–conserving terms in the decay amplitude. The information about CP symmetry is hidden in the polarization of virtual photon from $\eta \rightarrow \pi^+\pi^-\gamma^*$. The virtual photon converts into $e^+e^-$ pair ($\gamma^* \rightarrow e^+e^-$) and its polarization manifests itself in the asymmetry in the distribution of angle $\phi$ between pions and leptons emission planes. The graphical definition of dihedral angle is show in Fig. 2.2.

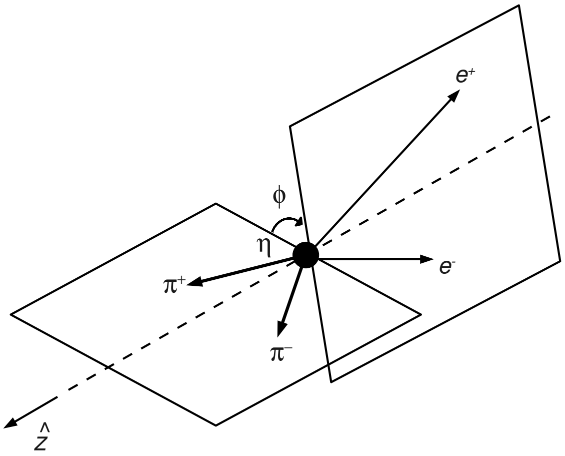

Figure 2.2: Graphical definition of the dihedral angle between the $\pi^+\pi^-$ and $e^+e^-$ emission planes.

The $e^+e^-$ pair will be emitted dominantly towards direction perpendicular to the photon polarization vector, while the number of particles emitted in the polarization planes will be much smaller [15]. The CP violation can manifest itself in an asymmetry around 90°. The fact that CP conservation requires the symmetry around $\phi = 90°$ can be also demonstrated graphically as it is shown in Fig. 2.3.

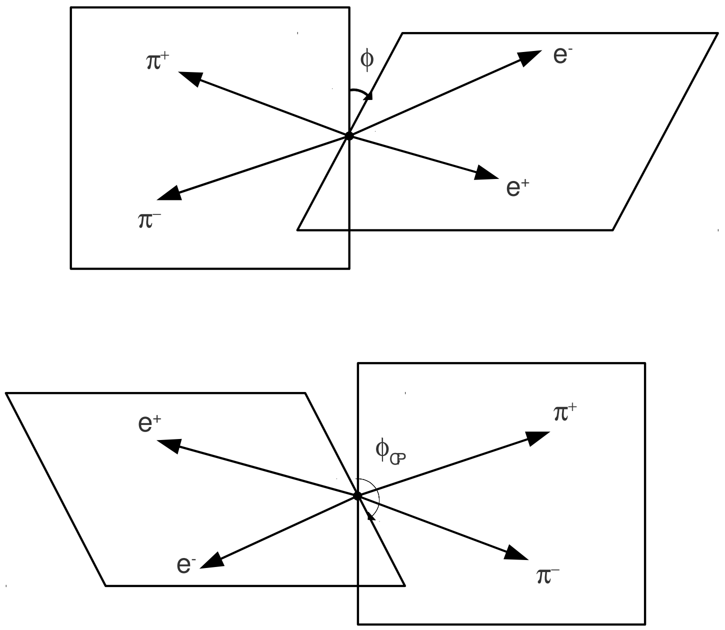

Figure 2.3: CP transformation. (Upper panel) – initial state of $\pi^+$,$\pi^-$,$e^+$,$e^-$, dihedral angle between the $\pi^+\pi^-$ and $e^+e^-$ emission plane. (lower panel): lower part represents the CP transformation done to the $\pi^+\pi^-e^+e^-$ system from the upper panel. After CP transforamtion $\phi_{CP} = 180° - \phi$

The level of this effect can be studied by measuring the number of $\pi^+\pi^-$ and $e^+e^-$ pairs emitted in angle $\phi$ and $180° - \phi$. As a quantitative measure of the CP violation one may use asymmetry defined as follows:

$$A_\phi = \frac{N_{0°<\phi<90°} - N_{90°<\phi<180°}}{N_{0°<\phi<90°} + N_{90°<\phi<180°}} = \frac{N_{\sin\phi\cos\phi>0} - N_{\sin\phi\cos\phi<0}}{N_{\sin\phi\cos\phi>0} + N_{\sin\phi\cos\phi<0}}, \tag{2.3}$$

where N denotes number of events, $\phi$ is the dihedral angle in the $\eta$ rest frame with $\sin\phi\cos\phi$ part expressed as follows:

$$\sin\phi\cos\phi = \frac{1}{2}\sin 2\phi = (k_{e^+e^-} \times k_{\pi^+\pi^-}) \circ z\,(k_{e^+e^-} \circ k_{\pi^+\pi^-}) \tag{2.4}$$

where $k_{e^+e^-}, k_{\pi^+\pi^-}$ are versors perpendicular to $e^+e^-$ and $\pi^+\pi^-$ emission planes in the $\eta$ rest frame, respectively. The asymmetry has been predicted on the level $1.3 \cdot 10^{-3}$ [16] using the experimental [17] constraint on coupling constant $g_{\eta\pi^+\pi^-}$ less than 0.12 MeV.

### 2.3.1 Box and triangles anomalies

The PVV (pseudoscalar-vector-vector) triangle anomaly (Fig. 2.4a) is responsible for the two–photon decay of the light pseudoscalar mesons $\pi^0, \eta$ and $\eta'$. The amplitude of the $\eta \to \pi^+\pi^-\gamma^*$ decay is determined by parameters of both the PVV triangle (Fig. 2.4a) and the PPPV (pseudoscalar–pseudoscalar–pseudoscalar–vector) box anomaly (Fig. 2.4b). However, the $\pi^+\pi^-\gamma^*$ decay mode of the $\eta$ is dominated by PVV $\eta \to \rho\gamma$, obscuring a direct signal from processes involving the box anomaly.

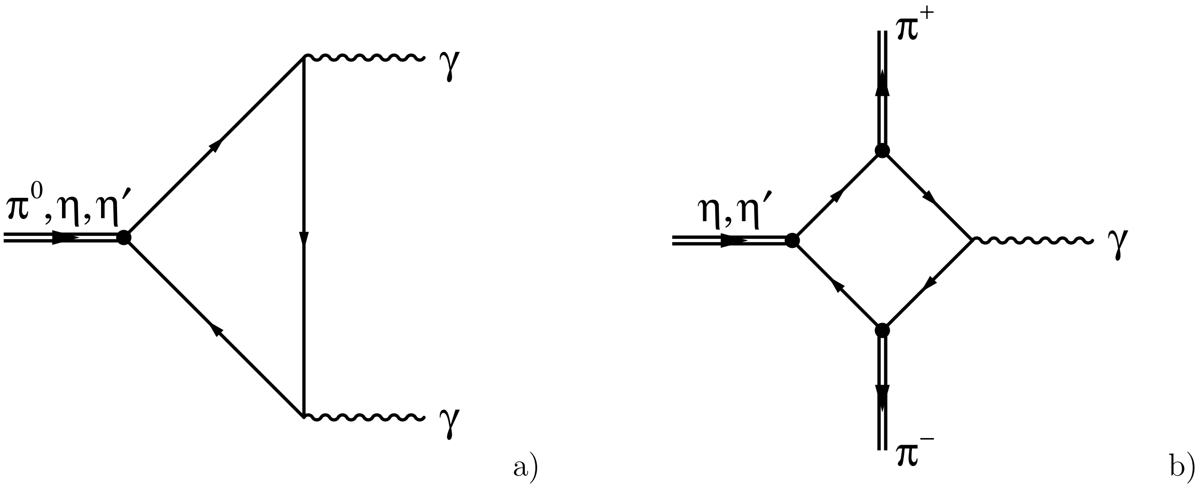

Figure 2.4: Anomalies in radiative decays of pseudoscalar mesons: (a) (PVV) Triangle anomaly, and (b) (PPPV) box anomaly.

In the Chiral Perturbation Theory the triangle anomaly is accounted for by the Wess–Zumino–Witten (WZW) term of the effective Lagrangian [18, 19].

### Chiral Unitary Approach

The standard expansion of **Ch**iral **P**erturbation **T**heory is not sufficient to successfully describe $\eta$ and in particular $\eta'$ decays. In order to obtain a realistic description of $\eta$ and $\eta'$ meson decays the final state interaction, which involves the formation of resonances, has to be taken into account [20].

The decay $\eta \to \pi^+\pi^- l^+ l^-$ has been recently studied using this framework [21]. The predicted invariant mass of the two pions is presented in Fig. 2.5.

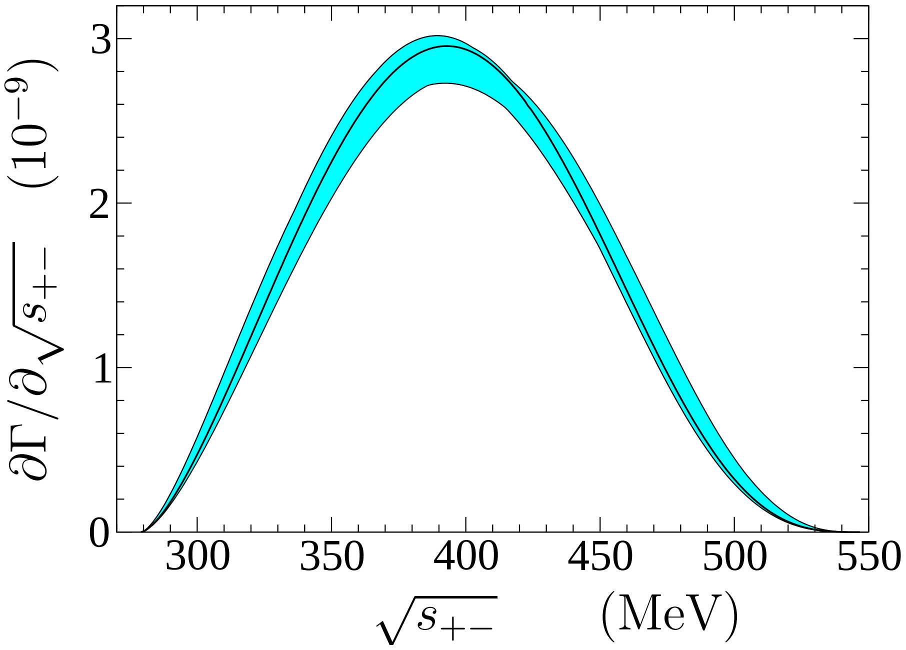

Figure 2.5: Calculated invariant mass of the $\pi^+\pi^-$ system for the $\eta \rightarrow \pi^+\pi^-e^+e^-$ decay. The solid line represents predictions of the chiral unitary approach [21] with parameters fitted to the experimental data, the error bands correspond to the $1\sigma$ confidence region from a fit to $\eta, \eta' \rightarrow \pi^+\pi^-\gamma$ partial decays widths.

## 2.4 Form factor

Electromagnetic processes involving photons and mesons reflect the coupling of photons to the electric charges of the quark fields. Therefore these processes may deliver information about the charge distribution inside the meson. The electromagnetic meson structure is described by the form factor, which is, in the non–relativistic case, related to the charge density distribution by a Fourier transformation. The form factor $\mathrm{F}\left(\mathrm{q}^2\right)$ can be determined comparing experimental results on the differential cross section with the exact calculation for a pointlike particle. For charged particles, electron scattering experiments (Fig. 2.6a) and $e^+e^-$ annihilation processes (Fig. 2.6b) allow to study charged pion form factor in the whole physically accessible range of four momentum transfer complementarily (for an introduction see [22]).

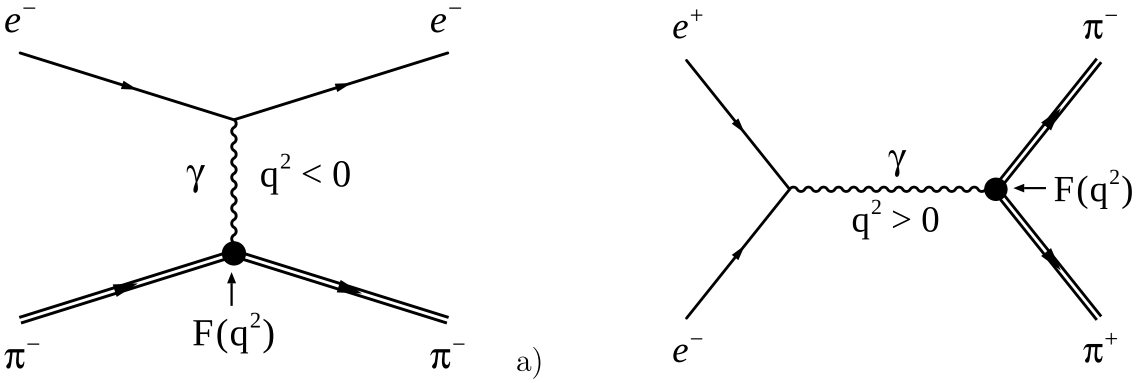

Figure 2.6: One–photon exchange processes and $\pi^{\pm}$ form factor F(q$^2$): (a) Space–like exchange in $e^-\pi^- \rightarrow e^-\pi^-$ scattering, and (b) time–like process in $e^+e^- \rightarrow \pi^+\pi^-$ annihilation.

In electron scattering on a charged meson (e.g. $e^-\pi^- \rightarrow e^-\pi^-$ shown in Fig. 2.6a) , the momentum transferred by the exchange of photon is given by the difference between the squares of the changes in energy and momentum of the electron. The *space–like* process is characterized by negative four momentum transfer squared:

$$\mathrm{q}^2 = (\Delta \mathrm{E}_e)^2 - (\Delta \mathrm{p}_e)^2 = -\,(\Delta \mathrm{p}_e)^2 < 0\,, \tag{2.5}$$

since in elastic collisions the electron energy remains unchanged, and only the direction of the momentum changes. The *time–like* process corresponds to positive $q^2$. The differential scattering cross section is given by

$$\frac{d\,\sigma}{d\,\mathrm{q}^2} = \left[\frac{d\,\sigma}{d\,\mathrm{q}^2}\right]_{pointlike} \left[\mathrm{F}\left(\mathrm{q}^2\right)\right]^2\,, \tag{2.6}$$

where $\left[\frac{d\sigma}{d\,\mathrm{q}^2}\right]_{pointlike}$ can be calculated using Quantum Electro–Dynamics. In annihilation processes (e.g. $e^+e^- \rightarrow \pi^+\pi^-$ in Fig. 2.6b) the square of the four–momentum of the intermediate virtual photon is equal to the invariant mass of the lepton–antilepton or meson–antimeson pair and therefore such process permits to study the form factor in the *time–like* region since

$$q^2 = M^2_{e^+e^-} > 0. \tag{2.7}$$

For neutral pseudoscalar mesons, the scattering process with single photon exchange of Fig. 2.6a is forbidden due to C–parity, which is conserved in strong and electromagnetic interactions. Consequently, the electromagnetic form factors of such mesons and hence their internal structure can only manifest itself in radiative decays into a photon and meson of opposite C–parity, e.g. in decays into a vector mesons and the photon, as shown in Fig. 2.7. The photon can be either real or virtual, in the latter case (Fig. 2.7) with a subsequent decay into a lepton pair $l^+l^-$ (*internal conversion*) where the square of the invariant mass $\mathrm{m}_{l^+l^-}$ of the lepton pair ($l = e, \mu$) is equal to the square of the four momentum of the virtual photon.

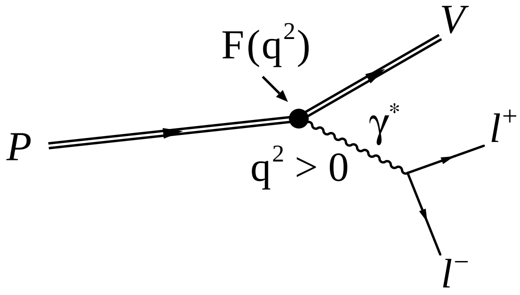

Figure 2.7: Diagram for decay of a pseudoscalar meson $P$ into a vector meson $V$ and an intermediate $\gamma^*$ converting to a lepton-antilepton pair.

The lepton invariant mass distribution depends on the electromagnetic structure at the transition vertex, which is due to a cloud of virtual states, i.e. the corresponding *transition form factor* describes transition dynamics rather than static properties as in the case of the electromagnetic form factor.

Thus in case of the reaction $\eta \to \pi^+\pi^-e^+e^-$ after normalization to the $\pi^+\pi^-\gamma$ decay width the lepton pair mass spectrum can be expressed as below [22]:

$$\frac{d\,\Gamma\left(\eta \to \pi^+\pi^-e^+e^-\right)}{d\,\mathrm{q}^2 d\,\Gamma\left(\eta \to \pi^+\pi^-\gamma\right)} = \Gamma\left(\eta \to \pi^+\pi^-\gamma\right)\left[\frac{d\,\Gamma\left(\eta \to \pi^+\pi^-e^+e^-\right)}{d\,\mathrm{q}^2\left(\eta \to \pi^+\pi^-\gamma\right)}\right]_{pointlike}\left|\mathrm{F}_{\eta(\pi^+\pi^-)}\left(\mathrm{q}^2\right)\right|^2, \qquad (2.8)$$

with QED term for a pointlike meson given by :

$$[...]_{pointlike} = \frac{\alpha_{em}}{3\,\pi}\sqrt{1-\frac{4\mathrm{m}_e^2}{\mathrm{q}^2}}\left[1+\frac{2\mathrm{m}_e^2}{\mathrm{q}^2}\right]\frac{1}{\mathrm{q}^2}\left[1+\left(\frac{\mathrm{q}^2}{\mathrm{m}_\eta^2-\mathrm{M}_{\pi\pi}^2}\right)^2-\frac{4\mathrm{m}_\eta^2\mathrm{q}^2}{\left(\mathrm{m}_{\eta^2}-\mathrm{M}_{\pi\pi^2}\right)}^{2}\right]^{\frac{3}{2}}, \qquad (2.9)$$

where $m_e, m_\eta$ are the electron and $\eta$ meson mass and $M_{\pi\pi}$ denotes the invariant mass of the two–pion system. The QED term leads to a strong enhancement in the invariant mass distribution at the lowest values of $q$. Form factor is expected to modify the distribution mainly at large $q$, like it is presented in Fig. 2.8.

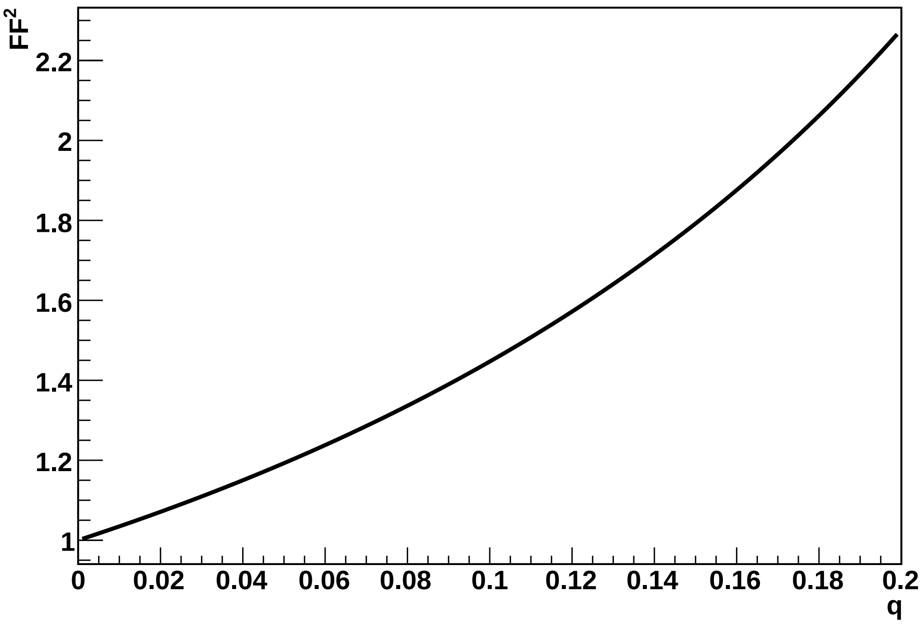

Figure 2.8: The Form factor squared (vertical axis) versus invariant mass $q$ in $[\frac{GeV}{c^2}]$(horizontal axis) based on the model from the reference [23].

At present it is not possible to calculate exactly the form factor in the Quantum Chromo Dynamics [24]. Therefore calculations of transition form factors are available from purely phenomenological models such as for example vector meson dominance (see [22]) or dynamical quark triangle loop models [25, 22], or from Chiral Perturbation Theory (for more information about the $\eta$ transition form factor see e.g. [26, 24]).

# Chapter 3

# WASA–at–COSY detector facility

WASA[1] detector was first proposed in 1987. The facility has been installed at The Svedberg Laboratory in Uppsala in 1998 as an internal experiment at the CELSIUS accelerator. The operation has been finished in 2005 and data collected are under evaluation [27, 28].

In 2006 the WASA facility was transferred from Uppsala to the Research Center Jülich in Germany and was installed at the **CO**oler **SY**nchrotorn COSY. The first production run there took place in April 2007. This chapter describes the detector facility including parameters of the target system and the super–conducting solenoid.

## 3.1 COoler SYnchrotron COSY

A storage ring named the cooler synchrotron COSY [29] is designed to accelerate protons and deuterons beams. The device is operated by Institute of Nuclear Physics (IKP) at the Research Center Jülich. The accelerator scheme is presented in Fig. 3.1.

---

[1] **W**ide **A**ngle **S**hower **A**pparatus

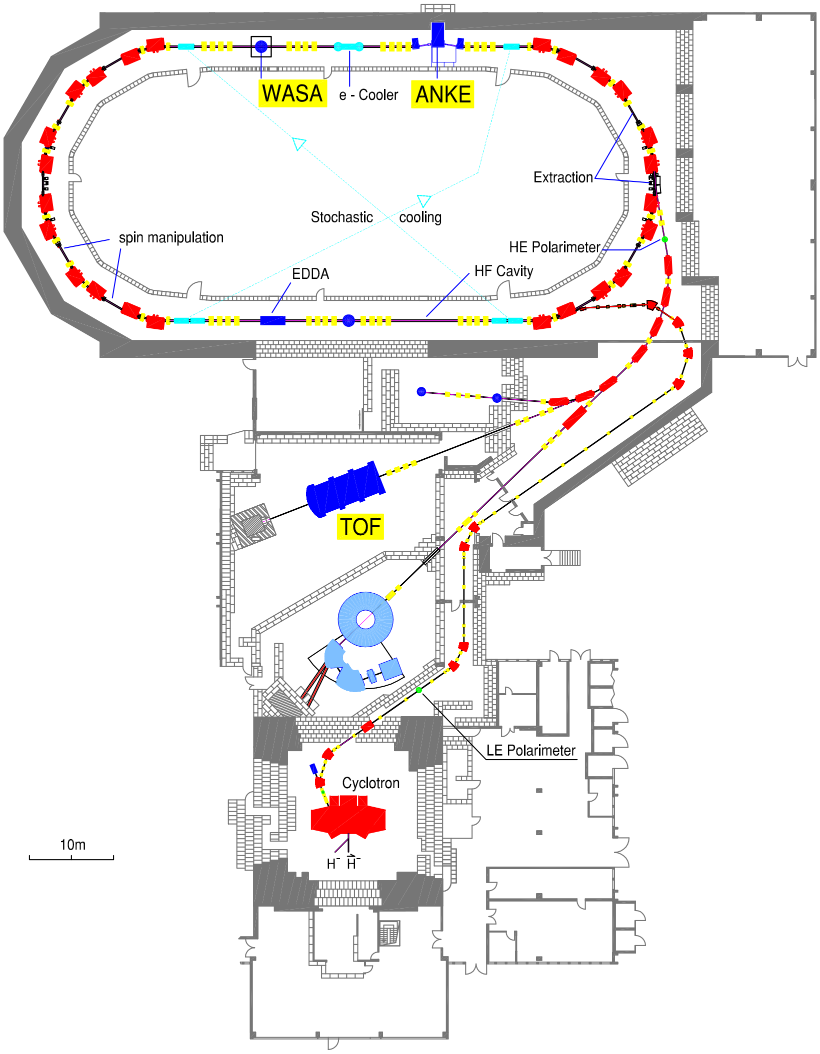

Figure 3.1: COoler SYnchrotron COSY. The scheme view of the COSY accelerator facility. Only presently active internal and external experiments are shown in the scheme: ANKE [30], TOF [31], and WASA [32]. Experiments: EDDA [33], PISA [34], COSY–11 [35], NESSI [36], BIG KARL [37], JESSICA [36] have finished measurment activity but data collected are under evaluation.

The ions $H^-$ and $D^-$ are preaccelerated in the in JULIC cyclotron up the momentum of 300 $\frac{MeV}{c}$. Next the beam is extracted and guided through 100 m long beam line to the injection in the storage ring. The COSY is equipped with electron and stochastic cooling systems [38] which are used to decrease the emittance and momentum spread of the beam. The main characteristics of COSY are given in Table 3.1.

| **The COSY storage ring** | |
|---|---|
| total length | 183.4 $m$ |
| momentum range | $0.3\ \frac{GeV}{c} - 3.7\frac{GeV}{c}$ |
| beam diameter | $\sim 4\ mm$ |
| intensity for protons | $\sim\ 10^{10}$ |

Table 3.1: The main parameters of the COSY accelerator.

For more details concerning the accelerator properties the interested reader is referred to references [38]

## 3.2 WASA detector

The WASA detector is built out of four main components: Central Detector, Forward Detector, Pellet Target System and the Scattering Chamber. The scheme of the detector is shown in Fig. 3.2. The functioning and calibration methods of the detector components were described extensively in many previous articles [32, 39, 40] and PhD theses [41, 42]. Therefore, in this work it will be only briefly reported and for details the interested reader is referred to the above mentioned publications.

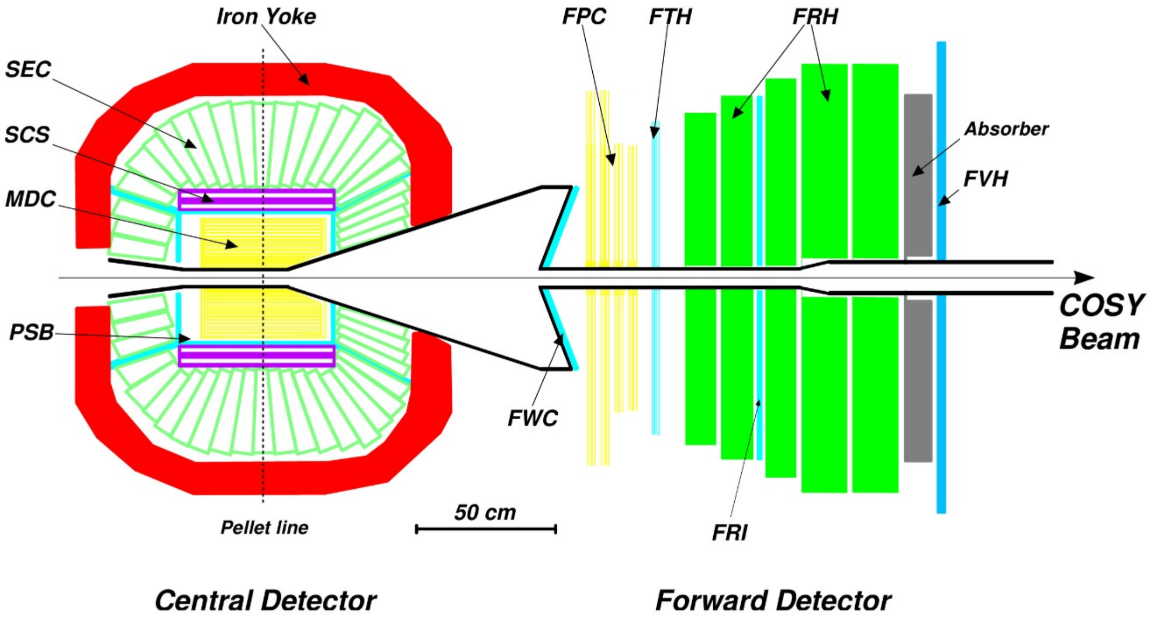

Figure 3.2: The side view of the WASA facility. For the description and the explanation of the detector's name abbreviations see text.

### 3.2.1 Pellet target

The main components of the target are placed in the top of the platform of the central detector. This target provides a narrow stream of very small frozen hydrogen or deuteron droplets called pellets. A jet of liquid hydrogen or deuterium is broken up into droplets by a vibrating nozzle. The pressure and temperature in the droplet chamber are below hydrogen triple point providing stability of pellets due to freezing of their surface in the evaporation. Before entering the scattering chamber the stream of pellets is collimated by means of 7 *cm* long vacuum cappilar. At the interaction region the areal thickness of pellets stream can reach $5 \cdot 10^{15}\ \frac{atoms}{cm^2}$. Figures 3.3 and 3.4 show target system.

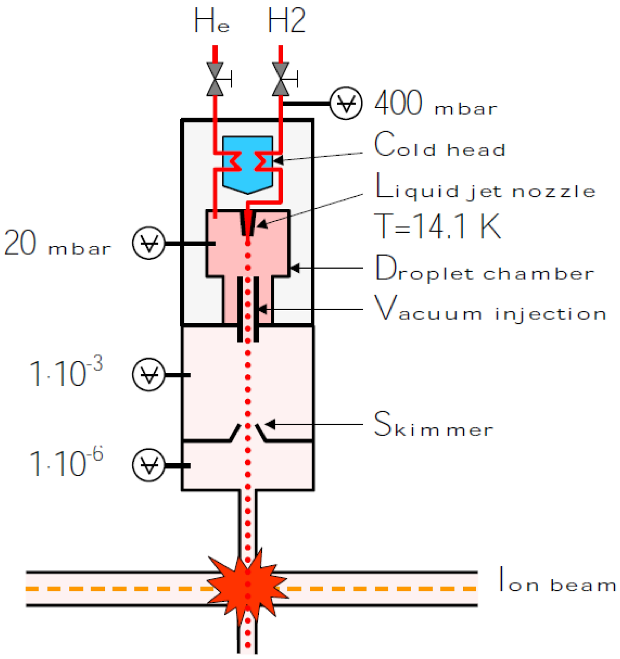

Figure 3.3: The scheme of the pellet target.

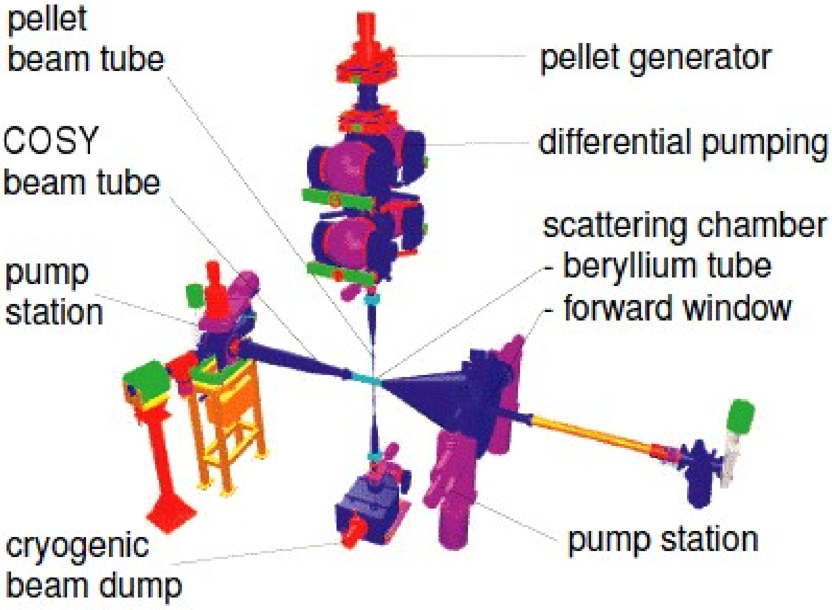

Figure 3.4: Overview of the whole pellet arrangement used in the WASA facility.

The main specifications of pellet target are summarized in table 3.2.

| **The pellet target** | |
|---|---|
| Pellet size | 25–35 $\mu m$ |
| Pellet frequency | 50–150 $kHz$ |
| Effective thickness | $> 10^{15}\ \frac{atoms}{cm^2}$ |
| Pellet stream diameter at beam | 2–4 $mm$ |

Table 3.2: The main characteristics of the pellet target

### 3.2.2 Scattering chamber

Since the WASA detector was designed to measure rare decays of mesons, the precise tracking of charged particles is of crucial importance and therefore, the scattering chamber is made out from Beryllium with a thickness of 1.2 $mm$. This allows to minimize probability of gamma external conversion and the energy and angular tagging of the charged particles. The photography of the chamber is shown in Fig. 3.5

Figure 3.5: Berylium scattering chamber together with a thin pipe for the pellets stream.

### 3.2.3 Central Detector

The central detector surrounds the interaction region and it is used for detection, identification and momentum reconstruction of neutral and charged ejectiles. As it was shown in Fig. 3.2 there are four components constituting the central detector (see Fig 3.6): **M**ini **D**rift **C**hamber (MDC), **P**lastic **S**cintillator **B**arrel (PSB), **S**cintillator **E**lectromagnetic **C**alorimeter (SEC), and **S**uper **C**onduction **S**olenoid (SCS). The central part of the WASA detector is visualised in Fig 3.6.

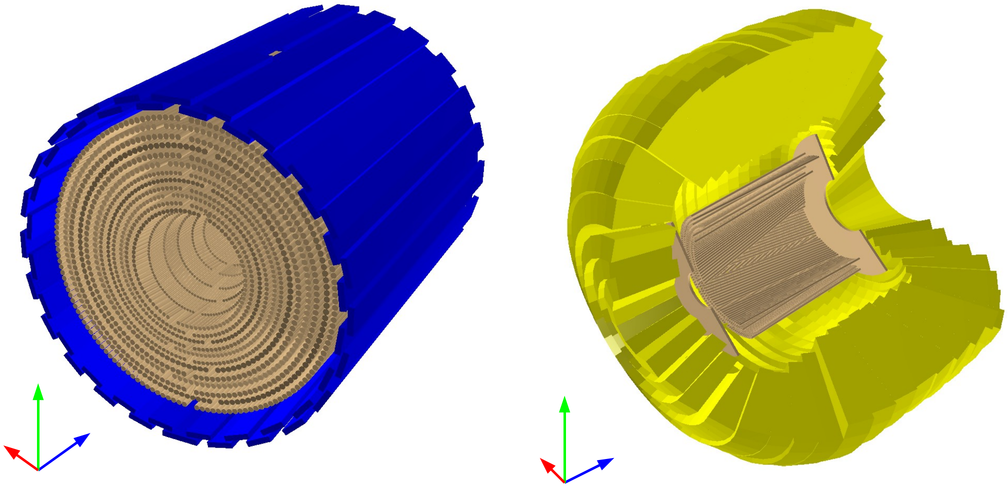

Figure 3.6: 3–D demonstration of the central detector elements: (right) outer part – the electromagnetic calorimeter, (left) inner part – mini drift chamber surrounded by plastic scintillator.

### Solenoid

The **S**uper **C**onducting **S**olenoid encircles MDC and PSB detectors and it provides axial magnetic field to separate charged ejectiles and to determine their momenta. In addition it protects the CD from low energy delta electrons created in the beam interaction with the pellets. The ending part of the SCS chimney is extended by a yoke, made out of pure irons with very low carbon content. This design provides protection of the calorimeter and shields the readout electronic from the magnetic field. The distribution of the magnetic field density is shown in Fig. 3.7 and main parameters characterizing SCS are listed in Table 3.3

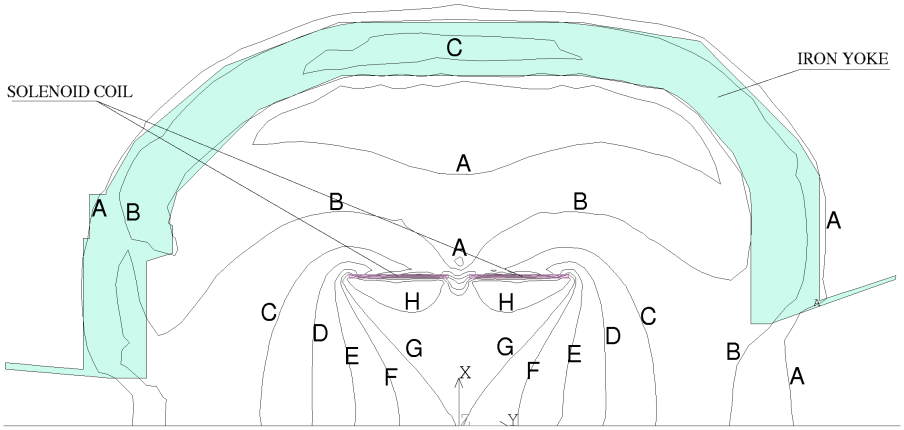

Figure 3.7: Map of the magnetic fields in the WASA experiment [43]. Marked contours indicate regions of the magnetic fields: A = 0.1T, B = 0.25T, C = 0.50T, D = 0.75T, E = 1.00T, F = 1.20T, G = 1.30, H= 1.50 T. The beam direction is orientated perpendiculary to the picture plane.

| **Coil** | |
|---|---:|
| Superconductor (stabilizer) | NbTi/Cu (Al) |
| Total lenghth | 465 *mm* |
| Field uniformity in the MDC | 1.22 $T \pm 20\%$ |
| Cooling | Liquid He, 4.5 *K* |
| Outer/inner radius | 288.8/267.8 *mm* |
| Wall tickness | 0.18 *mm* |

Table 3.3: . The characteristics of the super conducting solenoid.

### Mini Drift Chamber

The MDC is the cylindrical proportional straw detector surrounding the scattering chamber on the distance up to 0.5 $m$. It consists of 1738 thin–walled straws mylar[2] tubes arranged in 17 layers with the diameter range starting from 41 to 203 mm for inner and outer layer, respectively. Geometry of the detector provides the operability under high luminosities up to $10^{32}\ \frac{1}{cm^2 \cdot s}$. MDC permits the reconstruction of the track curvature in the magnetic field (see Fig. 3.7) and so allows to determine momentum of the outgoing charged particles. Detailed description of the chamber is available in [44].

#### Plastic Scintillator Barrel

The Plastic Scintillator Barrel is placed inside Super Conduction Solenoid and surrounds the Mini Drift Chamber. The cylindrical shape with additional forward and backward part allows to cover full scattering angle. The detector delivers fast signal used in the trigger system. It is used to distinguish between charged and neutral particles and moreover it serves as a $\Delta E$ detector in the $\Delta E - E$ and $\Delta E - P$ technique for the identification of charged particles.

### 3.2.4 Forward Detector

Forward Detector of the WASA–at–COSY facility covers the region of the polar angle from 3 to 18 degrees. It consists of plastic scintillators components for the charged hadron identification and tracking detectors for determination of their trajectories. Main parts are briefly presented in the following section and general properties are summarized in table 3.4

| **Forward Detector** | |
|---|---|
| Scintillator elements | 340 |
| Scattering angle coverage | $3° - 18°$ |
| Angular resolution | $0.2°$ |
| Provided identification | $\Delta E - E$ |
| Maximum stopping power:<br>$\pi^{\pm}/d/p/\alpha$ | 170/400/300/900 $MeV$ |

Table 3.4:
The most important parameters of the Forward Detector.

---

[2] Biaxially–oriented polyethylene terephthalate (boPET) polyester film is used for its high tensile strength, chemical and dimensional stability, transparency, reflective, gas and aroma barrier properties and electrical insulation.

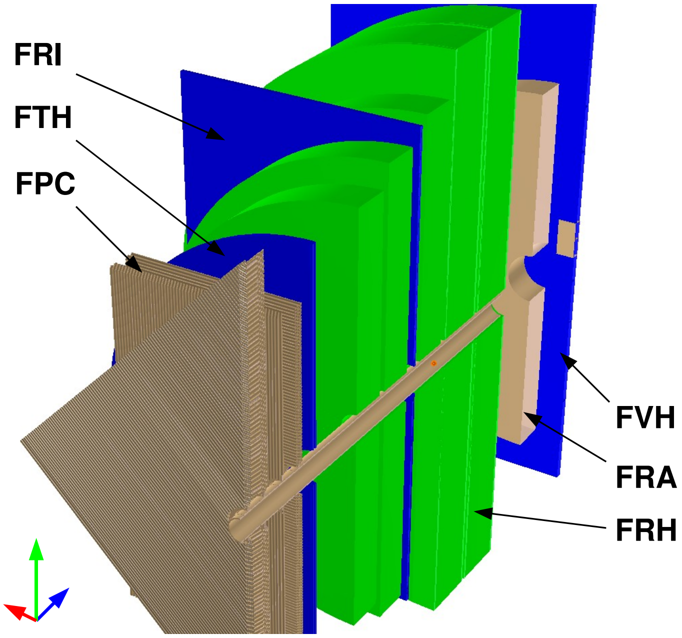

Figure 3.8: The half of the forward detector cross section. The abbreviations on the picture are explained in text.

### The Forward Window Counter (FWC)

Forward Window Counter is a segmented plastic scintillator detector placed in the minimal distance in the forward cone to the scattering chamber (see Fig. 3.2). It consists of two planes each with 12 elements covering full azimuthal polar angle, 30° per element. FWC is used in the first level trigger logic.

### The Forward Tracker (FPC)

Downstream the beam the Forward Proportional Chamber called "tracker" is placed. It delivers information about direction of the momentum vector of ejectiles leaving the scattering region from $3^\circ - 23^\circ$ with respect to the beam line. Detailed description of the detector is presented in chapter 4.

### The Forward Trigger Hodoscope (FTH)

The Forward Trigger Hodoscope (see Figs 3.2 and 3.8) detector consists of 3 layers of scintillators. There are 24 Archimedes spiral arcs located in the first two layers and 48 radial elements arranged in the third plane. Coincident detection of signals in all three layers gives one pixel per particle passing, minimizing the ambiguity of multi–hit events. Since the timing of the hit can be determined by FTH with accuracy better than 1 $ns$ the device is used inside low level trigger logic.

### The Forward Range Hodoscope (FRH)

The Forward Range Hodoscope is used for the determination of the energy of the forward scattered charged particles and for their identification. Together with FTH it allows to realize the $\Delta E - E$ method of the particle identification. The detector is build out of 5 layers (3 with 11 $cm$ and 2 with 15 $cm$ thickness) which permits determination of stopping power of registered particles and finally determination of their kinetic energy. The energy resolution for protons with the kinetic energy 0.35 GeV ends up in 1-2% but in the punch–through particles case the reconstruction of energy is less accurate.

### The Forward Veto Hodoscope (FVH)

The Forward Veto Hodoscope constitutes last two layers of the Forward Detector. It is build out of 12 plastic scintillator bars equipped with photomultipliers on both sides. In the first layer bars are arranged horizontally and in the second layer vertically. Combination of signals form Forward Range Hodoscope and Forward Veto Hodoscope allows to reject punch through particles.

## 3.2.5 Data acquisition

The WASA–at–COSY detector is designed to work with high luminosities up to the level of $10^{32}\ \frac{1}{cm^2 s}$. The electronic contains 2500 ADC and 8000 TDC–channels. The typical length of the recorded event amount to 5 $kbytes$. The WASA–at–COSY data acquisition allows to read out up to 10 $kHz$ events. The way of the information processing is schematically demonstrated in Fig. 3.9 [45, 46].

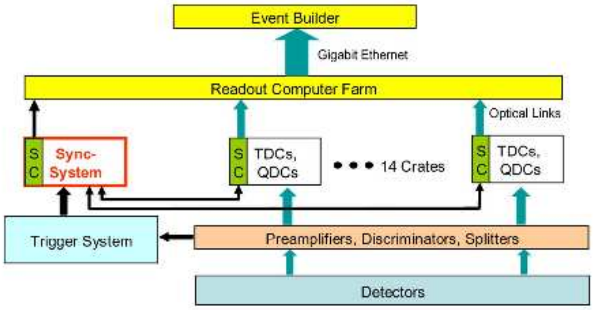

Figure 3.9: The scheme of the WASA–at–COSY acquisition system.

The WASA–at–COSY trigger is based on signals from scintillators with clustering of neighboring detectors [47, 48]. A multiplicity is calculated for each detector plane. The trigger electronics allows to define also the multiplicity of tracks by counting number of "matching hits" which corresponds to the hit in consecutive layers in FWC–FTH–FRH with the same azimunthal angle $\phi$.

The analog photomultipliers (PMT) signals from the electromagnetic calorimeter are summed in groups of 4x4 or 3x4 before being sent to a dual threshold discriminator. Two energy thresholds are applied giving logic signals for both high and low energy. The signals from the groups are matched with signals from the plastic scintillator to get information on the particle charge. Finally the multiplicity of groups for the different cases of charged, neutral, high or low energy are calculated. The analog signals can be further summed allowing to set a threshold on the total energy in the electromagnetic calorimeter or in its subsections, e.g. the right or left half.

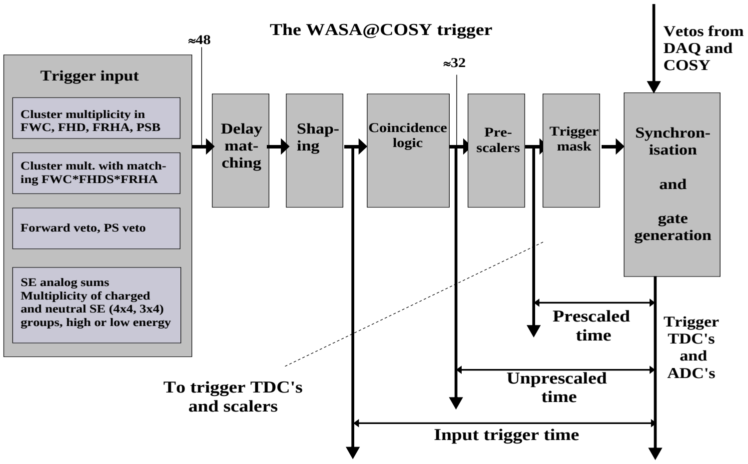

Figure 3.10: The trigger system applied in the WASA–at–COSY experiment.

At present up to 32 different coincidence conditions, "triggers", can be programmed simultaneously. The 32 triggers can optionally be prescaled to allow for high rate monitoring triggers to be included in the data stream. Finally a mask "AND" "OR" units selects the triggers that are allowed to start the readout. The logic units were developed at Uppsala University for the WASA-CELSIUS experiment [39]. Many parameters like delays, coincidence conditions, prescale factors and mask can be remotely programmed via an $I^2C$ [3] bus built into the trigger crates.

The logic of the event processing is schematically depicted in Fig. 3.10

---

[3] A multi–master serial computer bus designed by *Philips*. The connection is mainly used to attach low–speed peripherals to a motherboard, system, or cellular phone.

For the measurement of the reaction described in this thesis a following trigger condition has been applied: The event required one or more clusters [4] in the first plane of the Forward Range Hodoscope and also no hit in the forward Veto Hodoscope. Additionally in the calorimeter there should be at least two clusters from charged particles passing the low energy threshold.

---

[4] Hits in adjacent detector belonging to incident particle.

# Chapter 4

# Forward Proportional Chamber

The Forward Proportional Chamber construction and calibration will be presented in more details in this thesis since it was a responsibility of the author to take care of the preparation of this detector[1] for the measurements at COSY.

The WASA–at–COSY detector is equipped with Mini Drift Chamber and Forward Proportional Chamber. They consist of 1768 and 1952 straw tubes, respectively. The straw is built of mylar coated cylinder of 4 millimeters radius with 26 $\mu m$ thickness and the sense gold plated wire along its axis. A high voltage of some kV is applied between the wire and the tube so that an electric field is present in the gas filled area in atmospheric pressure. Each tube works as small proportional gaseous detector. The single tube is often referred to as a straw detector. The single straw is held at ground potential and the applied voltage on the wire ($U_o$) creates an electric field of the form:

$$E\left(r\right) = \frac{U_o}{r \cdot ln\left(\frac{r_{straws}}{r_{wire}}\right)} \tag{4.1}$$

Charged particles passing through the cylinder create a certain number of electron–ion pairs. Due to the electric field the electrons drift towards the anode wire and the ions towards the cathode. Very close to the wire (within a few radii of the wire) the electric field becomes strong enough that the electrons gain enough energy to ionize other molecules in the gas. The produced new free electrons are accelerated and can produce next ion–electron pairs and so on. The result is an ionization avalanche. The induced signal on the wire depends on potential drop through which ions move. Most of electrons travel only through a very small potential drop because they are created very close to the wire, but the ions have to travel through almost the whole potential drop. As a result the signal is nearly entirely

---

[1] The tracking detectors have been developed in seventies [49, 50, 51, 52] and are still successfully used nowadays.

due to the motion of the positive ions.

This section provides overview of the working nature of straws chambers used and presents obtained results in the process of particles tracking in the WASA–at–COSY experiment.

## 4.1 Work and design

The Forward Proportional Chamber is a tracking detector for charged particles. It consists of four planes with sensitive area of about 92 × 92 $cm^2$ which are subdivided in two identical halves as demonstrated in Fig. 4.1. The whole chamber is equipped with 1952 straws. The arrangement of a single plane delivers information about one coordinate in the Cartesian frame. In order to measure both coordinates the direction of straws in neighboring planes is rotated by 90°. The diameter of a single straw is 8 $mm$, and each plane consists of four parallel layers of drift tubes. Each layer is shifted by a tube radius and tubes are adjacent to each other. The scheme of the plane cross section is presented in Fig. 4.2.

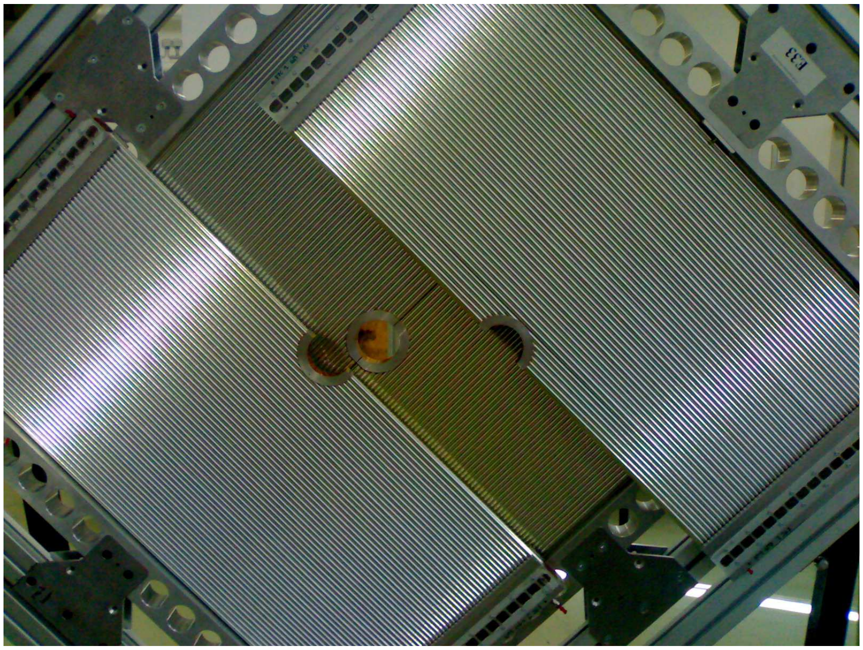

Figure 4.1: The Forward Proportional Chamber during the mounting procedure. Two halves are still separated.

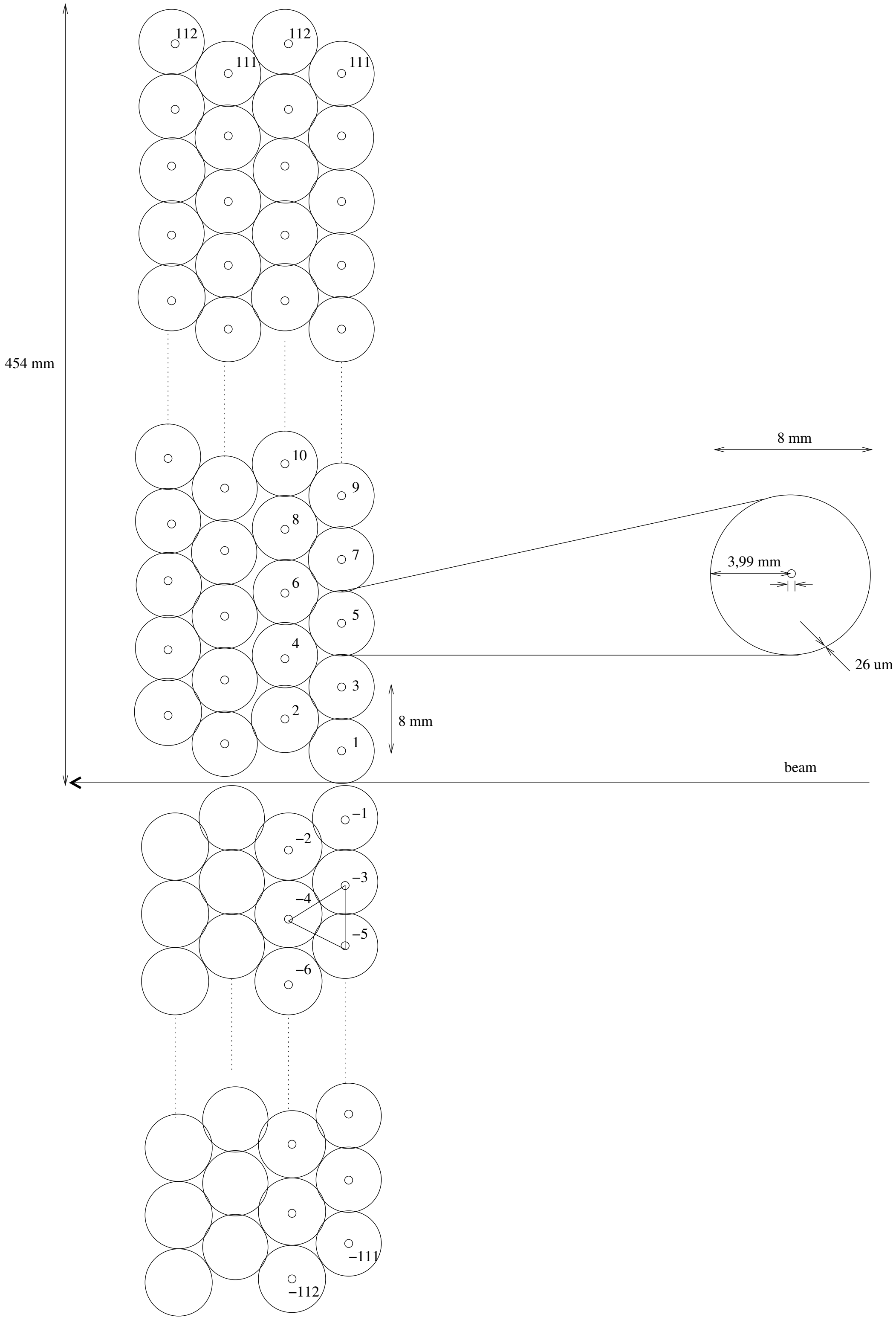

Figure 4.2: The geometrical scheme of the cross section of a single plane of the FPC. Marked digits indicate tube id as used by the decoding process during data taking.

All planes are positioned vertically with respect to the COSY accelerator beam tube which is used as a reference z–axis. The center of gravity of the FPC chamber is located in about 120 cm distance downstream from the interaction point.The tracker is designed to register particles outcoming from the interaction region with the scattering angle from 3°-23° in the forward direction.

## 4.2 Performance of the FPC

After transfer to Jülich all straws were inspected for possible aging effects due to the long operation at the CELSIUS accelerator and for possible damages during the transportation. A series of tests were performed and new front–end electronics were developed and tested. Chamber have been equipped with electronics which is in details discussed in this section.

### Electronic

In order to use a proportional chamber as a drift chamber it is necessary to have a time reference signal, typically from scintillator, which tells when a particle passes the detector. This scintillator should be placed very close to the straw layers, because the larger the distance the bigger the timing uncertainty caused by the distribution of velocities of the registered particles.

The difference between time of signals from the anode wire and scintillator is subsequently used to extract the distance the electron has traveled to the anode–sense wire.

The chamber has been equipped with newly developed electronics. The first innovation in comparison to the former setup was the amplification of the voltage signal readout from the detector transferred simultaneously with supplying high voltage. The amplifiers are based on the CMP16 [45] chip serving readout of 16 channels(see Fig. 4.3- 4.4) with ability of the data collection, approximately with frequency of 10 $kHz$. Scheme of connections of the amplifier module is shown in Fig. 4.5

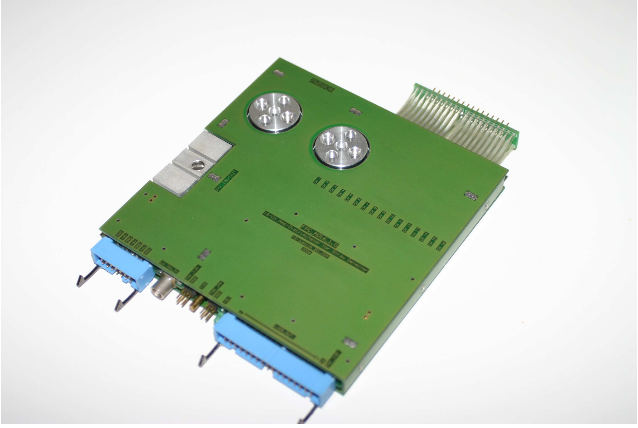

Figure 4.3: The mini CMP16 board. The mini version contains one preamplifier. The device has been mounted on the detector module to provide the readout of straws glued to the central metal piece (see Fig. 4.1).

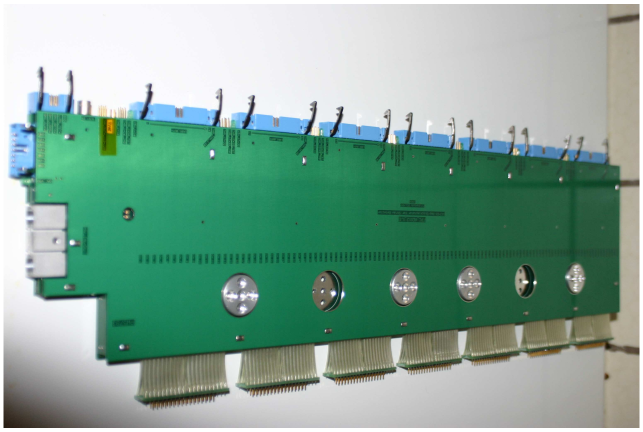

Figure 4.4: The CMP16 module. The long version is build out of 7 preamplifiers. It was designed to readout the whole plane with exception of straws glued to the central metal piece.

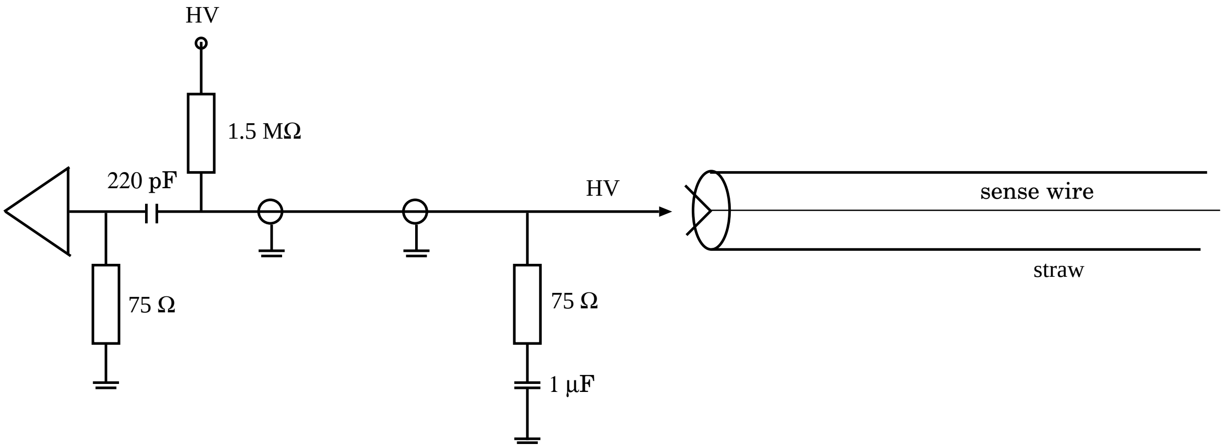

Figure 4.5: The connection of the CMP16 channel to the straw tube.

The signal from discriminator in LVDS standard is sent to the Time–to–Digital Converters (TDC) using 20 m twisted pair cables where logical information is translated to timing. Converters are built out of the newly designed components based on F1–chip. The single TDC module is shown in Fig. 4.6

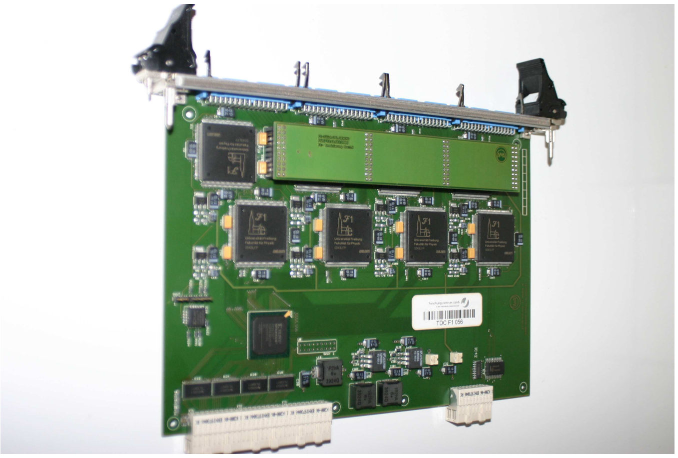

Figure 4.6: TDC module – readout.

### Test of the detector responses

The performance of each straw tube was investigated by inspecting the shape and amplitude of the analog signals. During these tests the straws were flushed with a 80/20 mixture of Ar and $C_2H_6$, and a voltage of 1.4 $kV$ was applied. The test revealed 1 % of dead channel. Those dead channels were not used in data analysis and also in the simulations. Since all remaining measured signal amplitudes were found to be reasonably similar there is no indication of strong local aging effects occurred during previous operation. Moreover, the gas flow conditions of all chamber components is satisfactory.

During data taking with cosmic rays prototype boards with CMP16 amplifier/discriminator chips were connected to an FPC module. The main goal of this test was to check the interoperability of the prototype CMP16 chips with the chamber module. The test was based on a measurement of the time between the signal from a scintillator detector situated near the FPC and the signal from the chamber. The obtained result showed, as expected that the range of the drift time amounts approximately to 130 $ns$.

### Gas system

The chambers are mostly supplied by noble gases which provide good multiplication in low electric field and avoid chemical reactions with sensitive components. The main difficulty of using such type of gases is the emission of photons during returning to the ground state. This problem can be suppressed by adding organic components like Carbon Dioxide ($CO_2$) or Ethane ($C_2H_6$) which can absorb and disperse the photon energy in non radiative way.

Chambers in the WASA–at–COSY experiment are operated with the gas mixture Argon and Ethane in proposition 80/20 providing linearity of the drift time – to drift distance relation (see part 4.3) with relatively low operating voltage. The FPC is supplied by the gas mixture in atmospheric pressure and the operation voltage has been set to level of 1.4 $kV$. Figure 4.7 presents the gas system used in FPC operation.

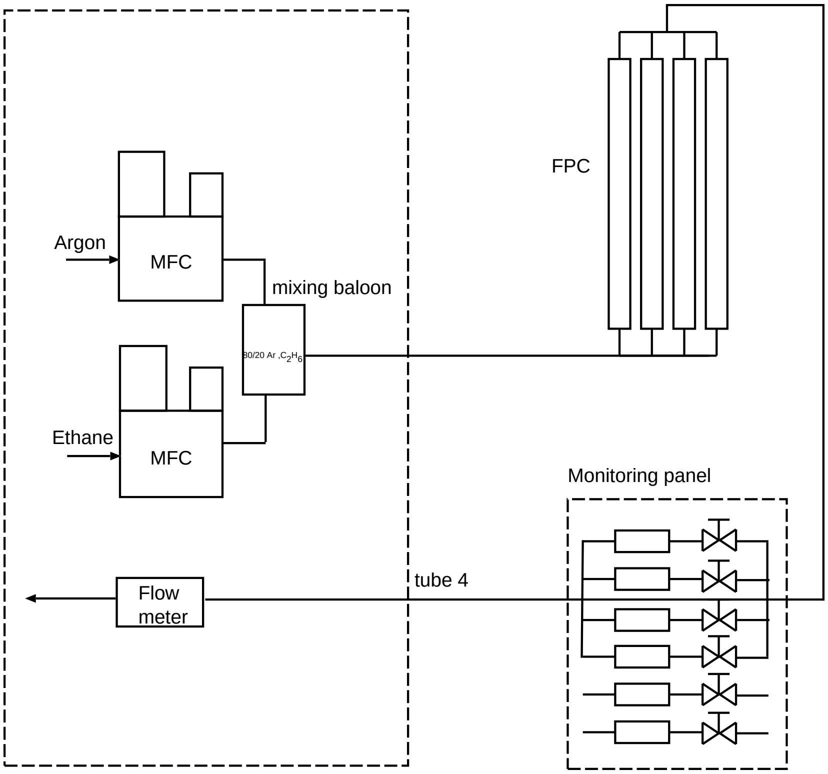

Figure 4.7: A block diagram of the FPC gas system.

The gas is distributed by the four channel Mass Flow Controller (MFC) to the mixing balloon. The mixture components have been set in percentage of gas flow in each channel separately. The complete mixture is provided to the detector via two polyethylene 8 meters tubes. The total gas flow has been set to 200 $\frac{ml}{min}$ to avoid gas loses and to compensate the flow resistance during the detector flushing. The gas goes out in similar way and the returning flow is monitored by flow meters. Such arrangement allows for monitoring a system against any possible leakages.

## 4.3 Calibration

FPC delivers time which is related to i) the time when particle passed through the straw, ii) the distance of particles trajectory from the sense wire and iii) to the velocity of ions and electrons produced in the ionization of the gas inside straws tubes. The calibration is the process of establishing a relation between drift time and the distance from sense wire referred to as drift distance. The full procedure is described in this section. The calibration have to be repeated every time the experimental condition had been changed. The calibration procedure is divided into three sub processes.

### T0 determination

The moment when particle penetrates the straw is provided by scintillator counter placed close to the chamber.

As a first step all time spectra are shifted with respect to each other in order to correct for the individual delays of readout electronic and signal cables. Time offsets have been found for each straw individually. As an example the distribution of the drift time for the seventh layer is shown in Fig. 4.8.

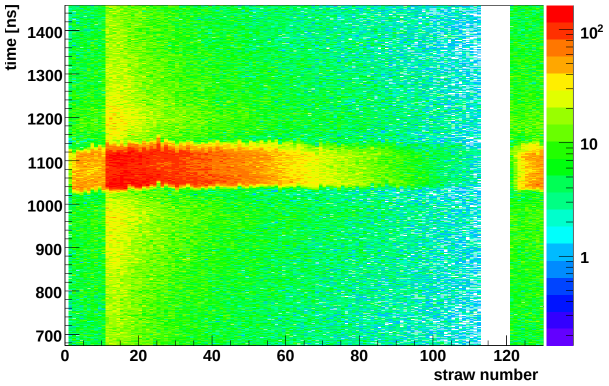

Figure 4.8: The distribution of the time difference $\Delta$T between T$_{FPC}$ and T$_{FTH}$ (y–axis) versus straw number of the seventh layer of the FPC tracker (x–axis). Straws around beam pipe starting from the number 1 to 12 and 121 and 131 respectively are glued to the central steel piece surrounding the beam pipe and readout only on one side. The numbers between 113 and 120 are not assigned to the straws.

The drift time is calculated as a difference between the time measured ($T_{FPC}$) from a given straw and the time from scintillator ($T_{FTH}$). This makes the determination of the drift time independent of the trigger timing. Finally the time offset signal is obtained for each straw by fitting to the leading edge of the drift time distribution a function of the form presented below:

$$f\left(x\right) = P_3 \cdot e^{\frac{1}{2}\left(\frac{(x-P_1)}{P_2}\cdot\frac{(x-P_1)}{P_2}\right)} \tag{4.2}$$

with $P_1$,$P_2$,$P_3$ being free parameters in the fit procedure. A typical drift time distribution from one layer is shown in Fig. 4.9

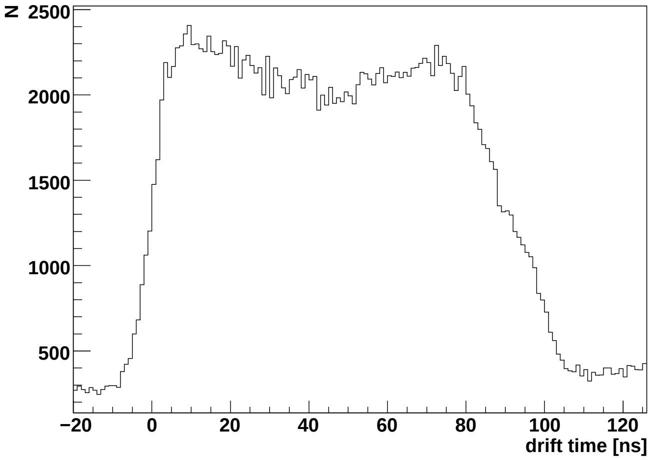

Figure 4.9: The summarized drift time distribution of all 130 straws from one half of the layer in the FPC.

### Determination of the drift distance

In the first approximation the drift time to distance dependence D(t) can be evaluated by the integration method valid under assumption of the homogeneous irradiation of the detector. Equation 4.3 presents the relation between the distance drift and time from the anode wire

$$D\left(t\right) = R_{wire} + \left(R_{tube} - R_{wire}\right) \cdot \frac{\int\limits_{0}^{t} N\left(t'\right) dt'}{\int\limits_{0}^{T_{max}} N\left(t'\right) dt'}, \tag{4.3}$$

where N is the number of events in the drift time spectrum at time $t$, $R_{tube}$ is inner radius of the straw and $R_{wire}$ is a radius of the wire equal to 35 $\mu$m. As a next step for each interval of drift time the distribution of differences between the distance to the wire determined from the calibration and from the reconstruction was established. Based on the mean of this distribution the calibration function was corrected. The procedure was repeated iteratively until the corrections become negligible. The radial distribution obtained after the calibration is presented in Fig. 4.10.

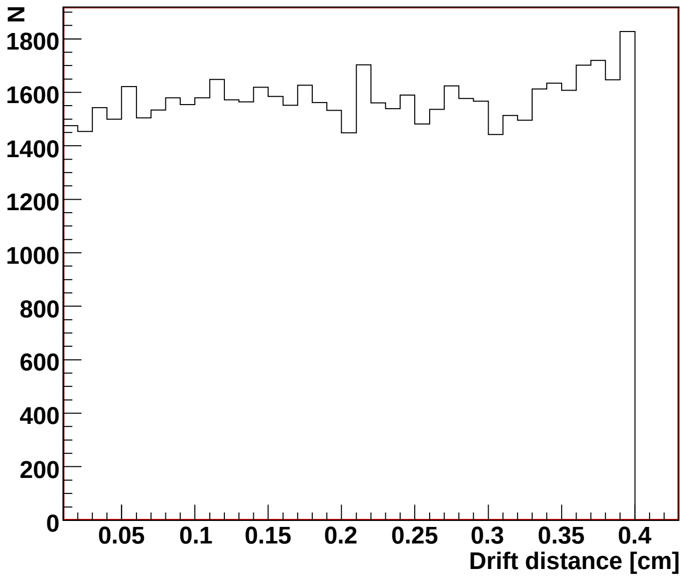

Figure 4.10: Distribution of the drift distance obtained as the final calibration result.

### Track reconstruction and final fitting

Based on the FPC signals the reconstruction of the particle trajectories can be performed. The *binary mode* based on the straw size and arrangement allows for processing the event and determine quickly track candidates. This method is used for on-line debugging of collected data and for the monitoring of chamber operability. Advanced mode based on the drift distance from the sense wire is used in the off-line analysis. It contains user independent packages available in RootSorter. The digital part is started by searching of the neighbors straws hit in one event and group of valid hits. At this stage the misidentified tracks are rejected by the projection of track candidates to the Forward Trigger Hodoscope detector where the hit position (determined based on the cluster signals) can be compared to the hit position established as the pixel in FTH. The hit pattern requires three or four layers of straws grouped into cluster. The clustering is done for all four FPC planes individually, so the track candidate contains all respective cluster combined by the track fitting routine. The calculation of track is done in two steps dependent on the level of precision. In the first approximation the center of hit is taken into account. In the second step the inclination angle of the track is established by the least-squares-fit method to the two–dimensional track.

## 4.4 Efficiency and resolution

Since no other device is available to externally measure the calibration and resolution of the FPC, the test was based on the comparison between distances to the sense wire determined from the calibration and from the reconstructed tracks. For this purpose events having hits in each layer and with only one hit per layer were selected. The tested layer was excluded from track reconstruction. In this manner the radius from calibration can be compared to the fitted radius given from independently reconstructed track. From the obtained distribution of differences between these radii the spatial resolution of straws can be derived.

### Internal chamber resolution

The corresponding distributions for four planes are shown in Fig. 4.11. The figure shows residuals defined as the difference between measured and fitted radii, expressed as follows:

$$R_i\left(t\right) = r_{i,fitted}\left(t\right) - r_{i,measured}\left(t\right) \tag{4.4}$$

where "i" is the number of straw and "t" denotes the drift time.

Taking into account plots 4.11 the internal chamber resolution can be studied. Residual spectra can be divided by certain region of wire radius and the $\sigma_{real}$ is obtained by Gaussian fit individually for radius slices. The average value of the $\sigma$ has been found to be about 330 $\mu m$ and it is independent of the drift time. It is worth to stress that this value is fairly in agreement with the resolution of MDC equal to 325 $\mu m$ as established in [41]. Figure 4.12 shows the relation between spatial resolution and distance from the sense wire. At this stage it is possible to check calibration quality by position of the residual which should be symmetric around zero. Otherwise the determination of the relation between the drift time and the drift distance should be corrected and one needs to perform the calibration procedure again until changes are negligible.

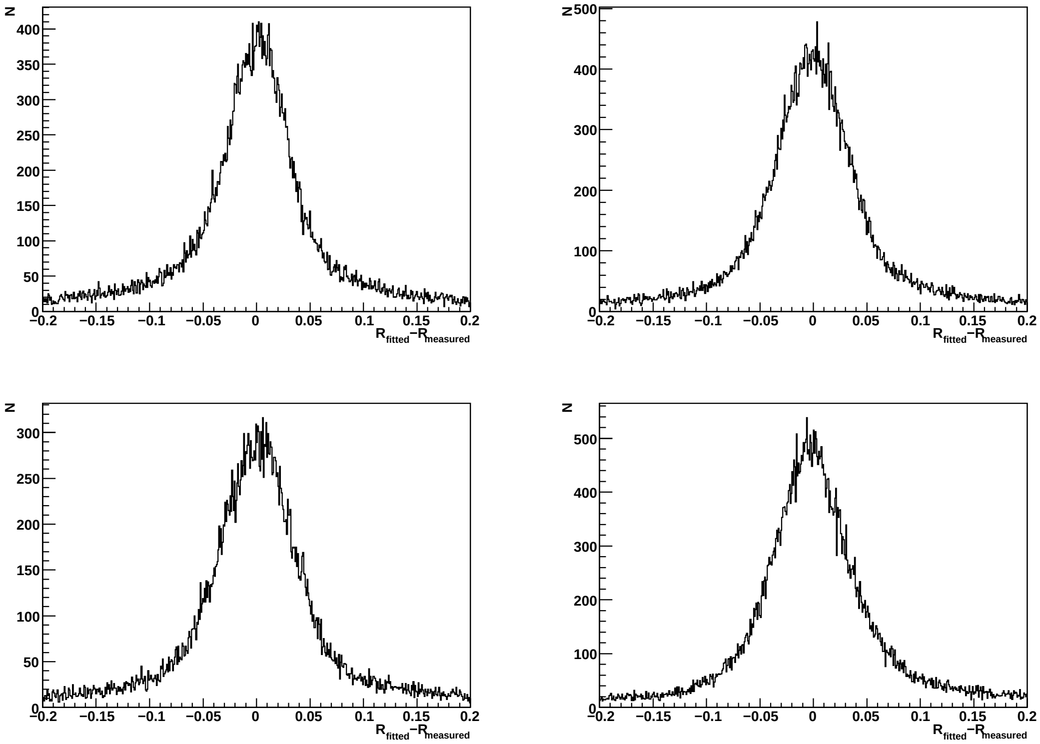

Figure 4.11: Distribution of residuals for four planes of FPC. On the horizontal axis the values are shown in centimeters. The figure illustrates that resolution was similar in all planes.

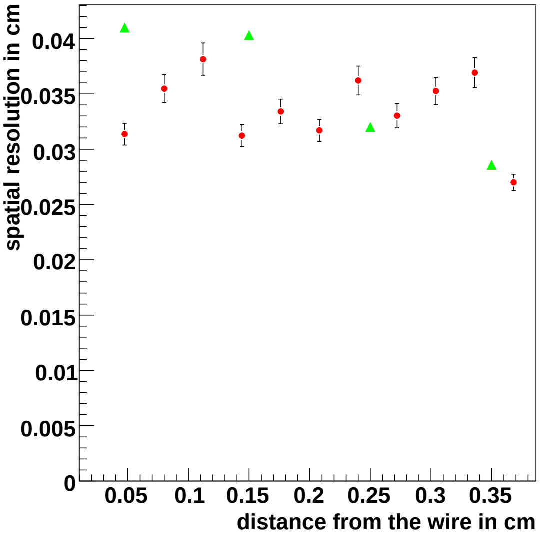

Figure 4.12: The spatial resolution ($\sigma$) as a function of distance to the wire. Red dots – data from WASA–at–COSY measurement, green triangles – data from WASA–at–CELSIUS.

# Chapter 5

# Off–line analysis

The off–line analysis processes have been started from decoding the data collected and stored in the hard disk resources of the analysis workstations of the WASA–at–COSY experiment.
The goal of the experiment is the determination of the signal from the $\eta \rightarrow \pi^+\pi^-e^+e^-$ decay channel. The analysis is based on the identification of the $^3He$ ions from signals in the Forward Detector and $\pi^+, \pi^-, e^+, e^-$ particles from signals in the Central Detector. Next the $\eta \rightarrow \pi^+\pi^-e^+e^-$ decay will be identified based on the missing mass of $pd \rightarrow^3 HeX$ reaction and invariant mass of the $\pi^+\pi^-e^+e^-$ system.

This part of the dissertation gives a brief review on the analysis tools and the interpretation of the data samples based on the Monte Carlo calculation.

### 5.0.1 Preselection

As the first criteria for selecting events corresponding to $pd \rightarrow^3\!He\ \eta \rightarrow^3\!He\ \pi^+\pi^-e^+e^-$ reaction chain one track needs to be registered in the Forward Detector and at least 28 tubes must give signals in the Mini Drift Chamber associated with corresponding clusters in the Plastic Scintillator Barrel. This is a minimum number of signals needed in the further analysis for reconstruction of four tracks in the Central Detector. Consistency of timing between time of a cluster [1] from Plastic Scintillator Barrel and the track found in the Forward Detector was checked. For this purpose the difference between average time in three layers of Forward Trigger Hodoscope and time of a cluster in the Plastic Scintillator Barrel was used (see Fig. 5.1).

---

[1] cluster is build out of neighbouring signals from detector modules on the software stage

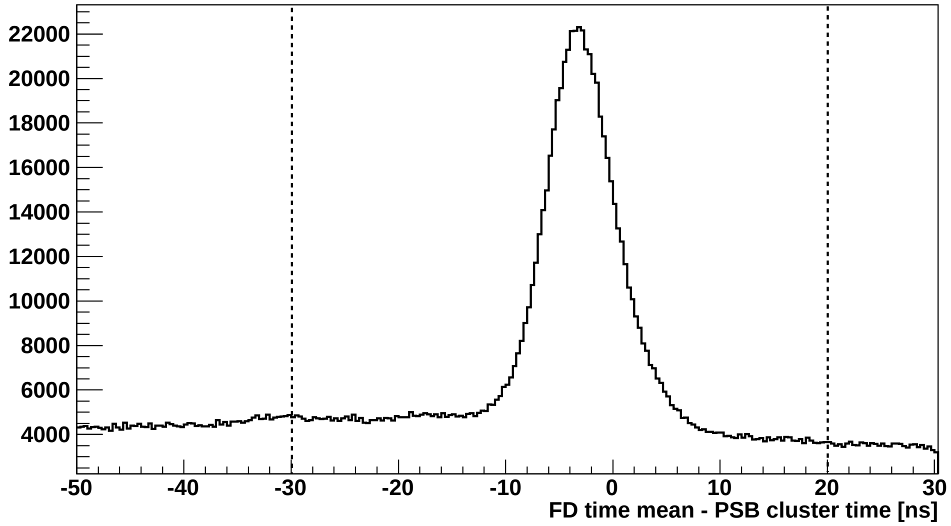

Figure 5.1: Time difference between time of a cluster in the Plastic Scintillator Barrel (PSB) and mean time in the Forward Trigger Hodoscope (FTH). Lines demonstrate the region of 50 $ns$ accepted for further analysis.

Events outside 50 $ns$ region were rejected. Such data sample has been prepared as the input to the advanced track reconstruction.

### 5.0.2 Track reconstruction

As the next step the reconstruction of tracks in the Mini Drift Chamber was performed. The geometrical overlaps between (i) Mini Drift Chamber, (ii) Plastic Scintillator Barrel and (iii) cluster in Electromagnetic Calorimeter have been checked and only tracks associated with clusters in Plastic Scintillator or Electromagnetic Calorimeter are processed. Additionally presence of clusters in the Electromagnetic Calorimeter not associated with any track has been permitted on this analysis stage. For the identification of the decay process $\eta \rightarrow \pi^+\pi^-e^+e^-$ four tracks are needed thus for the next step of analysis events with at least four tracks were taken into account. In addition, based on Fig. 5.2 a next cut on correlation in the time difference between the Forward Detector and Central Detector in the range from -14 to 8 $ns$ was applied.

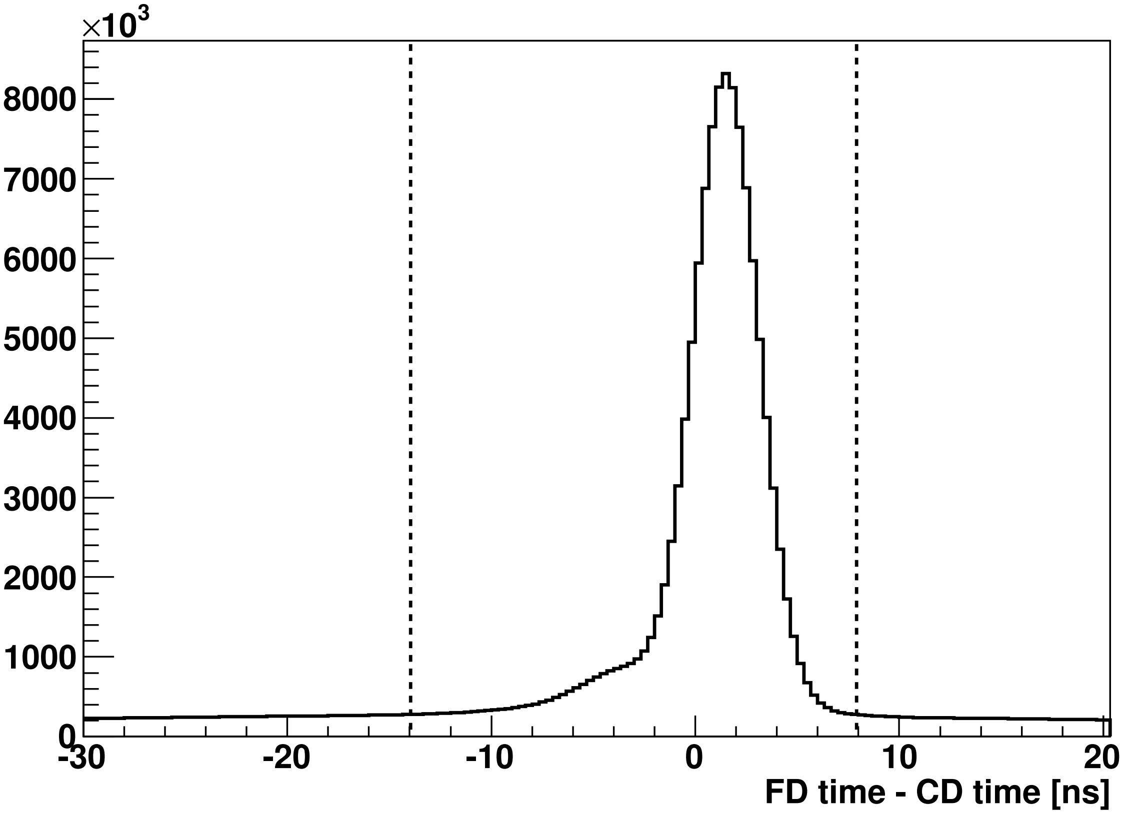

Figure 5.2: The time difference between signals caused by charged particles in Central and Forward Detector.

## 5.1 Particle identification

### 5.1.1 $^3$He ions

The $\eta$ meson is produced via the $pd \rightarrow ^3He\eta$ reaction. The helium is registered in the Forward Detector and it is identified based on energy loss ($\Delta E - E$) technique as demonstrated in Fig. 5.3. This figure shows the sum of energy deposited in the Forward Window Counter and the Forward Trigger Hodoscope versus the energy deposited in the first layer of the Forward Range Hodoscope. One can recognize the clear band of events corresponding to $^3He$ ions which are mostly stopped in the first layer of FRH and only a small fraction reach the second layer. Protons and deuterons are removed on the preselection level based on energy loss patterns in the five layers of the Forward Range

Hodoscope [53].

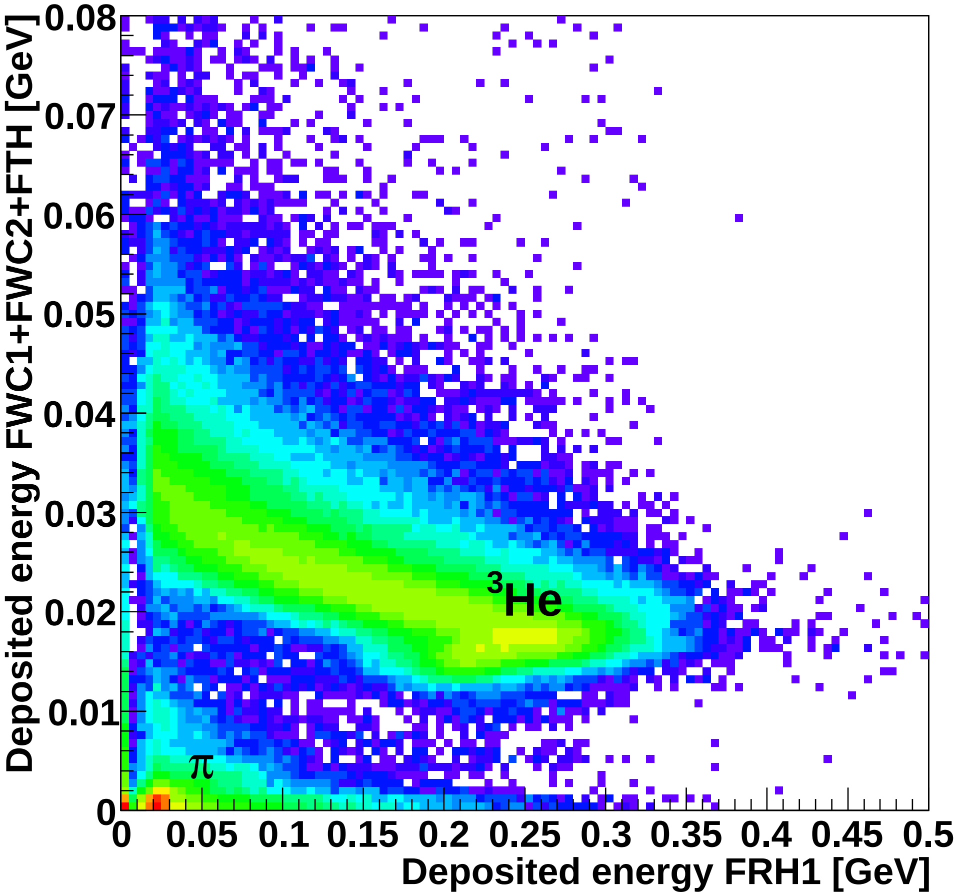

Figure 5.3: The sum of energy loss in the Forward Window Counter (FWC1, FWC2) and the first layer of Forward Trigger Hodoscope (FTH1) versus energy loss in the first layer of the Forward Range Hodoscope (FRH1).

After identification of events with $^3He$ the four momentum vector of $^3He$ was reconstructed based on its kinetic energy deposited in the Forward Detector and angles reconstructed from signals in the Forward Trigger Hodoscope. Next, using this information the missing mass of the $pd \rightarrow ^3He\ X$ reaction was calculated according to formula 5.1

$$m_x^2 = |\mathbb{P}_{beam} + \mathbb{P}_{target} - \mathbb{P}_{^3He}|^2, \tag{5.1}$$

where $\mathbb{P}_{beam}, \mathbb{P}_{target}, \mathbb{P}_{^3He}$ denote four momentum vectors of the proton beam, target, and the outgoing $^3He$ respectively. The missing mass distribution is presented in Fig. 5.4.

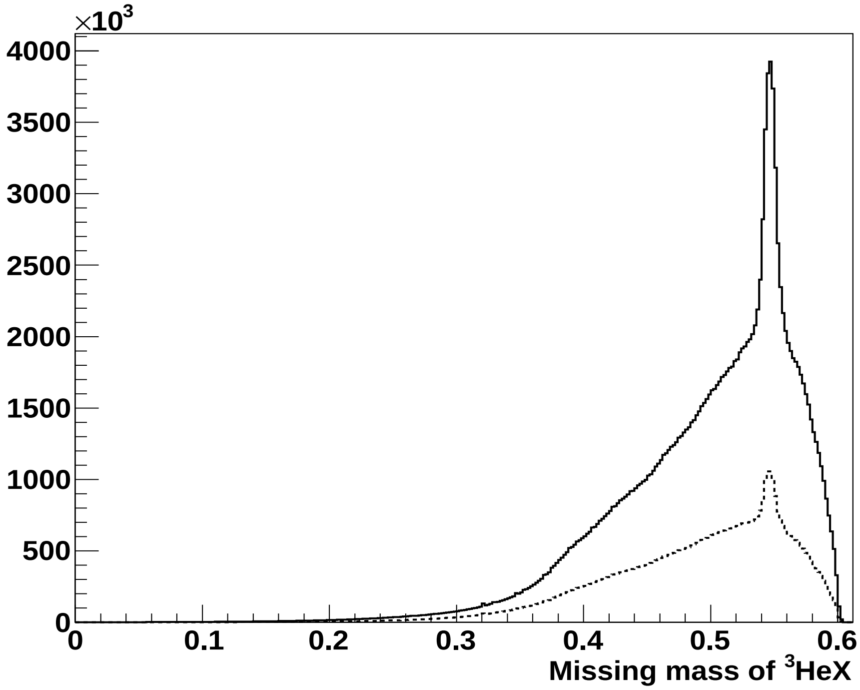

Figure 5.4: Solid line–the missing mass distribution to the $pd \rightarrow^3 He\ X$ reaction plotted without any constrain in the Central Detector. Dotted line represents the missing mass distribution under condition of event selection described in 5.0.1 (at least 28 signals in Mini Drift Chamber associated with clusters in the Plastic Scintillator Barrel.)

The obtained distribution reveals a clear peak at the value corresponding to the mass of the $\eta$ meson. The continuous background originates from the multi–pion production reactions. In order to estimate the number of reconstructed $pd \rightarrow ^3He\ \eta$ events the background was fitted outside the peak region by the sum of polynomial and Gauss functions. Next after subtraction of the fit result from the experimental spectrum a number of $pd \rightarrow ^3He\ \eta$ was estimated to $10816000 \pm 6700$.

### 5.1.2 Identification of the $\pi^+\pi^-$ and $e^+e^-$ pairs

The identification of electrons and pions is accomplished by employing a correlation plot of the energy deposited in Plastic Scintillator Barrel ($\Delta E$) or in the Electromagnetic Calorimeter ($E$) versus the momentum reconstructed based on the curvature of tracks measured in Mini Drift Chamber ($P$). In order to distinguish between the positively and negatively charged particles one assigns a negative or positive value of the momentum, depending on the curvature of the trajectory.

As the first step in order to determine regions corresponding to pions and electrons only events containing two charged tracks with balanced charge have been used. In addition in order to see the signal from electrons on the overwhelming pion "background" we have enhanced in the data sample the relative number of $e^+e^-$ pairs with respect to $\pi^+\pi^-$ pairs by making constraints that the opening angle must be smaller than 20 degrees. The choice of the cut at 20 degrees was motivated by the results of simulation shown in Fig. 5.5.

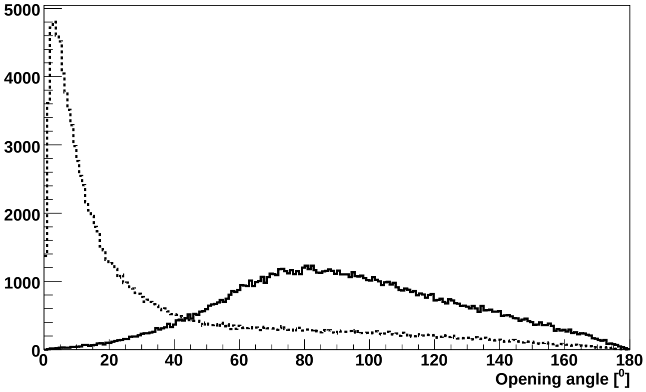

Figure 5.5: Monte Carlo simulations of opening angle between final state particles from the $\eta \rightarrow \pi^+\pi^-e^+e^-$ reactions. Dotted line – opening angle between electrons, solid line – opening angle between pions. The simulation has been performed assuming that the reaction proceeds via $\eta \rightarrow \pi^+\pi^-\gamma^* \rightarrow \pi^+\pi^-e^+e^-$ using a model presented in the reference [23].

In this picture one can see that the maximum of the opening angle distribution is around 80 degrees in the case of pions in contrast to electron–positron pairs which are boosted forward and this results in enhancement of the opening angle distribution close to zero degree.

The resulting histogram of $\Delta E - P$ for that sample of two track events with opening angle less than 20 degrees is shown in Fig 5.6.

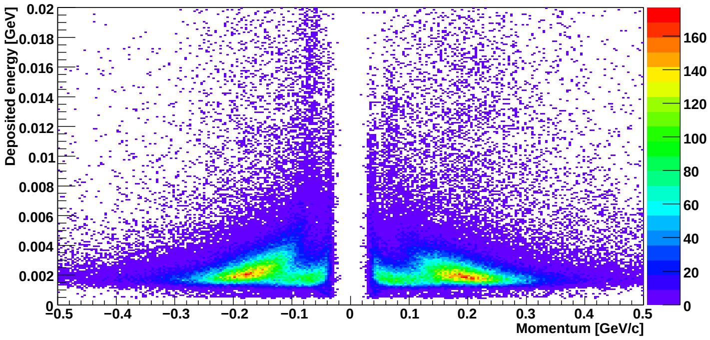

Figure 5.6: Identification of charged particles using the $\Delta E - P$ plot. Energy deposited in the PSB versus momentum reconstructed in the MDC.

One recognizes in the figure the enhanced density of events in the area corresponding to pions and electrons. Next the graphical region on the $\Delta E - P$ spectrum was defined as it is shown in Fig. 5.7.

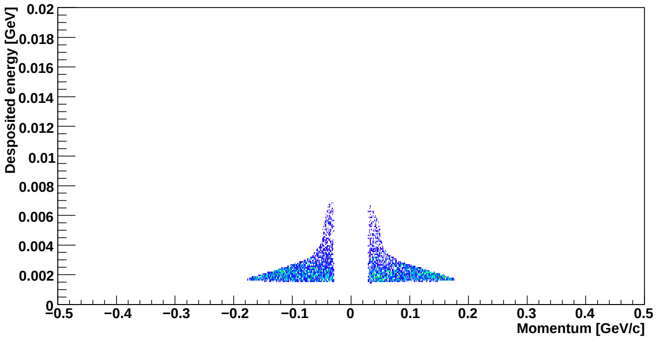

Figure 5.7: Identification of charged particles using the $\Delta E - P$ plot. Definition of the graphical region corresponding to leptons $(e^+, e^-)$, leftovers are consider like pions.

Electron mass is assigned to tracks corresponding to the interior of the marked region and the tracks corresponding to points from the outside of this region are considered as pions. It is important to stress that the two track events and the cut on the opening angle were used only in order to find the area on the $\Delta E - P$ plot corresponding to electrons. Having defined the criteria for the electrons and pions identification we have selected events with four tracks and out of them for the further analysis only these were accepted which were identified as $\pi^+\pi^-e^+e^-$.

### 5.1.3 Signature of the $pd \rightarrow^3He\ \eta \rightarrow^3He\ \pi^+\pi^-e^+e^-$ reaction

As a next step, in order to identify number of events corresponding to the $\eta \rightarrow \pi^+\pi^-e^+e^-$ decay candidates a missing mass spectrum to the $pd \rightarrow^3HeX$ reaction has been determined for these events for which in the Central Detector four tracks were reconstructed and identified as $\pi^+\pi^-$ and $e^+e^-$ pairs according to the method described in the section 5.1.2. The resulting missing mass distribution is presented in Fig. 5.8. One recognizes a clear peak at the missing mass value corresponding to the mass of the $\eta$ meson. It is worth to notice that at the present stage of the analysis the signal to background ratio is improved with respect to Fig. 5.4. The observed peak may be due to the $pd \rightarrow^3 He\ \pi^+\pi^-e^+e^-$ process but it may also partially be due to other reactions chains as summarized in table 5.1.

| **Background channels** | | |
|---|---|---|
| No. | Reaction | Branching ratio or cross section |
| 1 | $pd \rightarrow^3He\ \eta \rightarrow^3He\ \gamma\gamma$ | BR($\eta \rightarrow \gamma\gamma$) = ($0.3930 \pm 0.0020$) |
| 2 | $pd \rightarrow^3He\ \eta \rightarrow^3He\ \pi^+\pi^-\gamma$ | BR($\eta \rightarrow \pi^+\pi^-\gamma$) = ($0.0460 \pm 0.0016$) |
| 3 | $pd \rightarrow^3He\ \eta \rightarrow^3He\ e^+e^-\gamma$ | BR($\eta \rightarrow e^+e^-\gamma$) = ($0.0070 \pm 0.0007$) |
| 4 | $pd \rightarrow^3He\ \eta \rightarrow^3He\ \pi^+\pi^-\pi^0 \rightarrow^3He\ \pi^+\pi^-\gamma\gamma$ | BR($\eta \rightarrow \pi^+\pi^-\pi^0 \rightarrow \pi^+\pi^-\gamma\gamma$) = ($0.273 \pm 0.0028$)$\times$($0.98230 \pm 0.00034$) |
| 5 | $pd \rightarrow^3He\ \eta \rightarrow^3He\ \pi^+\pi^-\pi^0 \rightarrow^3He\ \pi^+\pi^-e^+e^-\gamma$ | BR($\eta \rightarrow \pi^+\pi^-\pi^0 \rightarrow \pi^+\pi^-e^+e^-\gamma$) = ($0.2273 \pm 0.0028$) $\times$ ($0.01174 \pm 0.00035$) |
| 6 | $pd \rightarrow^3He\ \eta \rightarrow^3He\ \pi^0\pi^0\pi^0 \rightarrow^3He\ \gamma\gamma\gamma\gamma\gamma\gamma$ | BR($\eta \rightarrow \pi^0\pi^0\pi^0$) = ($0.3200 \pm 0.0023$) $\times$ ($0.98230 \pm 0.00034$) |
| 7 | $pd \rightarrow^3He\ \pi^+\pi^-$ | cross section unknown |
| 8 | $pd \rightarrow^3He\ \pi^+\pi^-\pi^0 \rightarrow^3He\ \pi^+\pi^-e^+e^-\gamma$ | cross section unknown |
| 9 | $pd \rightarrow^3He\ \pi^+\pi^-\pi^0 \rightarrow^3He\ \pi^+\pi^-\gamma\gamma$ | cross section unknown |
| 10 | $pd \rightarrow^3He\ \pi^0\pi^0\pi^0$ | not well known |

Table 5.1: The background channels which may be missidentified as $^3He\ \pi^+\pi^-e^+e^-$ reactions.

Starting from the channels with associated neutral particles. Reaction No. 1 may contribute to

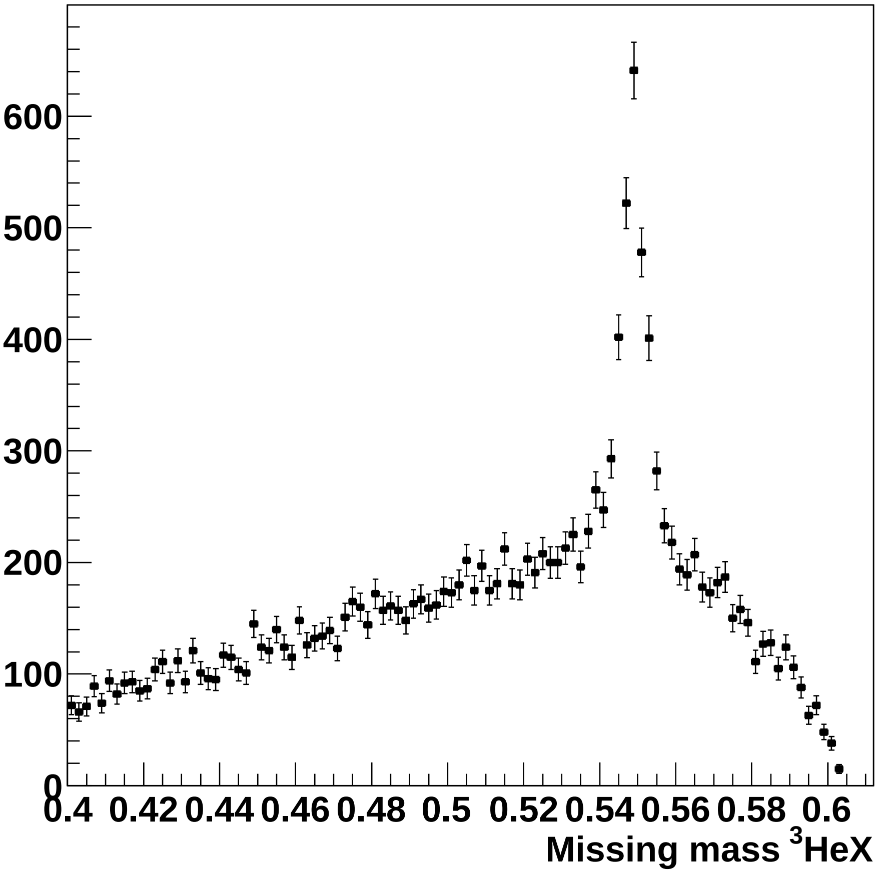

Figure 5.8: The missing mass distribution plotted in coincidence with four charged tracks corresponding to $e^+e^-$ and $\pi^+\pi^-$ pairs reconstructed in the Central Detector. The error bars denote statistical uncertainty.

the signal region in the case if both $\gamma$ convert to $e^+e^-$ pairs in the detector material and subsequently out of four leptons ($e^+e^-e^+e^-$) two will be misidentified as pions. Reaction No. 2 can fake the $^3He\ \pi^+\pi^-e^+e^-$ signal if $\gamma$ undergoes the external conversion in the detector material and the pions and leptons are identified correctly. The reaction No. 3 may be misidentified as the signal if photon undergoes the external conversion and subsequently one $e^+e^-$ pair is misidentified as $\pi^+\pi^-$. Reaction No. 4 can be misidentified with the $^3He\ \pi^+\pi^-e^+e^-$ final state if one of $\gamma$ converts in the detector material into $e^+e^-$ pair and the second $\gamma$ escapes the detection or merges with one of the signals from $\pi^+, \pi^-, e^+, e^-$. Reaction No. 5 may be reconstructed as $^3He\ \pi^+\pi^-e^+e^-$ signal if the $\gamma$ quantum appears analogously as in reaction No. 4.

In the case of $\eta$ meson decay into three neutral pions (No. 6) the $\pi^+\pi^-e^+e^-$ final state can be reconstructed if two of the pions would undergo the $\gamma\gamma$ decay and the $\gamma$ converts to $e^+e^-$ or escapes or gives signals below the threshold and one pair of $e^+e^-$ is misidentified as $\pi^+$ and $\pi^-$. Reactions No. 7 to 10 denote the prompt pion production which may also contribute to the signal due to the effects described above for reactions No. 1 to 6, with the difference however that the missing mass distribution from direct pion production will not be peaked at the mass value of the eta meson.

The absolute scale of the contributions from the background reactions to the measured missing mass signal can be obtained from the known number of the produced $\eta$ mesons.

For further discussion as an example let us consider reaction $pd \to ^3He\eta \to ^3Hee^+e^-\gamma$. The number of $pd \to ^3He\eta \to ^3Hee^+e^-\gamma$ events reconstructed as $^3He\ \pi^+\pi^-e^+e^-$ final state ($N^{\pi^+\pi^-e^+e^-}_{\eta\to e^+e^-\gamma}$) may be then determined as:

$$N^{\pi^+\pi^-e^+e^-}_{\eta\to e^+e^-\gamma} = N^{registered}_{\eta} \cdot BR_{\eta\to e^+e^-\gamma} \cdot P^{mi}, \tag{5.2}$$

where $P^{mi}$ denotes the probability of miss-identification of $e^+e^-\gamma$ state with $\pi^+\pi^-e^+e^-$. This may be estimated with Monte Carlo Methods by simulating signals of the WASA–at–COSY detector for $N^{MC}$ events of the $pd \to ^3He\eta \to ^3He\ e^+e^-\gamma$ reaction and calculating $P^{mi}$ as $\frac{N^{MC\ \pi^+\pi^-e^+e^-}_{\eta\to e^+e^-\gamma}}{N^{MC}_{reconstructed}}$ where $N^{MC\ \pi^+\pi^-e^+e^-}_{\eta\to e^+e^-\gamma}$ is the number of events reconstructed from the simulated sample as $^3He\ \pi^+\pi^-e^+e^-$ final state and $N^{MC}_{reconstructed}$ is the number of reconstructed $pd \to ^3He\eta$ events. Therefore, the expected number of events in the measured missing mass distribution from $pd \to ^3He\eta \to ^3Hee^+e^-\gamma$ is equal to:

$$N^{\pi^+\pi^-e^+e^-}_{\eta\to e^+e^-\gamma} = \frac{N^{registered}_{\eta} \cdot BR_{\eta\to e^+e^-\gamma} \cdot N^{MC\ \pi^+\pi^-e^+e^-}_{\eta\to\pi^+\pi^-e^+e^-}}{N^{MC}_{reconstructed}}. \tag{5.3}$$

Figure 5.9 shows the contributions listed in Table 5.1 where the spectra of the prompt production are described as the sum of polynomial and wide Gauss functions and the channels with the $\eta$ meson production and its subsequent decays were simulated taking into account known branching ratios (BR) and number of registered $\eta$ mesons as obtained in the experiment and scaled using the way presented above.

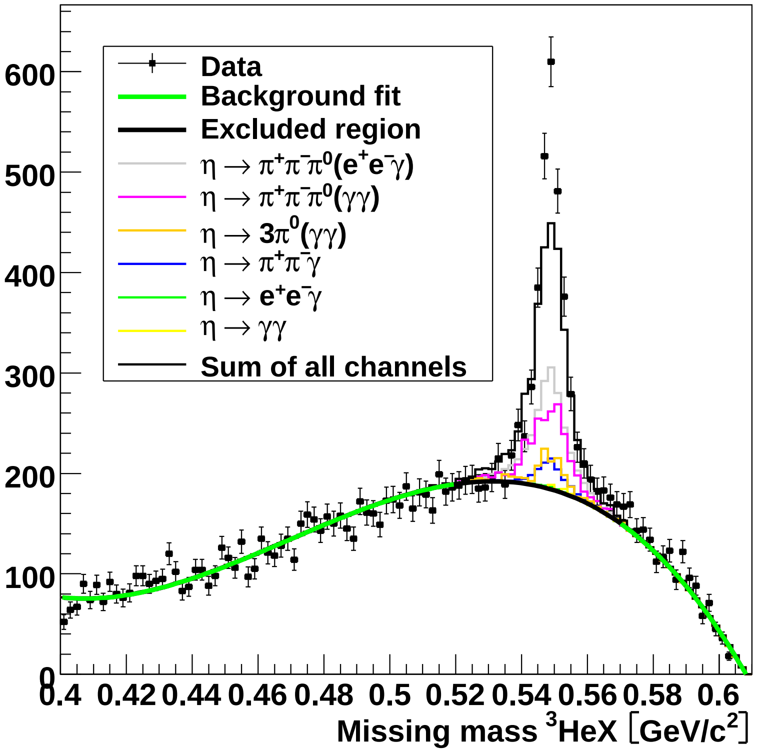

Figure 5.9: The missing mass distribution plotted in coincidence with four charged tracks corresponding to $e^+e^-$ and $\pi^+\pi^-$ pairs reconstructed in the Central Detector. Error bars denote statistical uncertainty. Solid line represent function used for the description of multipion contribution, the black–solid line region was excluded from the fit procedure. Contributions from $\eta$ decays are demonstrated in descending order starting from total background contributions, and further with $\eta \to \pi^+\pi^-\pi^0(e^+e^-\gamma), \eta \to \pi^+\pi^-\pi^0(\gamma\gamma), \eta \to 3\pi^0$, $\eta \to \pi^+\pi^-\gamma$, $\eta \to e^+e^-\gamma$, and ending with $\eta \to \gamma\gamma$.

## 5.2 Reduction of background

Constraints on the number of tracks and the balanced charge are not sufficient enough to exclude contributions originating from prompt (direct) processes and other decays of the eta meson. Thus as a next step background contributions from direct pion production and from the $\eta$ decays will be subtracted based on the missing mass spectrum.

### 5.2.1 Direct production of pions

Both processes, double and three pions prompt production form broad distribution in the missing mass spectrum for $pd \to^3 HeX$ reaction. As can be seen in Fig. 5.9, due to the misidentification of the final state particles prompt production of pions gives a significant contribution also to the missing mass spectrum for the final state reconstructed as $\pi^+\pi^-e^+e^-$. Cross sections for multipion production is not well known but the smooth shape of this kind of background on both sides under the $\eta$ signal allows to estimate its contribution to the $\eta$ peak by making a fit of the polynomial of 3th degree and Gauss function on both sides of the $\eta$ signal. The fit was performed for the data outside the range of the peak corresponding to the $\eta$ meson production. The spectrum after the subtraction of the contribution from the direct pion production is shown in Fig. 5.10.

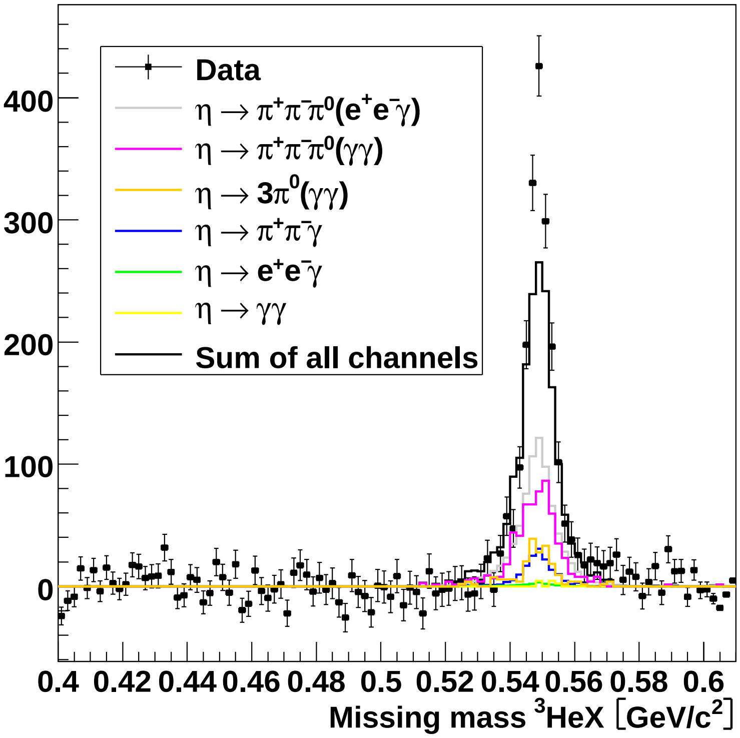

Figure 5.10: The missing mass spectrum after subtraction of distribution originating from continuous multipion background estimated by the function described in text. The order of lines is the same as in the Fig. 5.9, and as it is indicated in inserted legend. Only statistical error are shown.

Fig. 5.10 shows that the background from the $\eta$ decays constitutes still about 75 % of the peak.

### 5.2.2 Background from $\eta$ decays

The background channels from the $\eta$ decays listed in Table 5.1 cannot be distinguished from the $\eta \to \pi^+\pi^-e^+e^-$ decay based on the missing mass spectrum. Although, the missing mass distribution is significantly narrower than the distribution of the invariant mass, the invariant mass gives the possibility to decrease the background because the most decays of the $\eta$ meson have additional qamma quanta in respect to $\eta \to \pi^+\pi^-e^+e^-$ channel. The calculated invariant mass for the $\pi^+\pi^-e^+e^-$ decay is on the average always larger than for final state as e.g. $\pi^+\pi^-e^+e^-\gamma$ because energy of gamma is equal to its momentum and $(E - E_\gamma)^2 - (P - P_\gamma)^2 < E^2 - P^2$. Therefore, the invariant mass cut can effectively decrease the background decays with an additional gamma quantum as can be seen e.g. in Fig. 5.11 a,b,c.

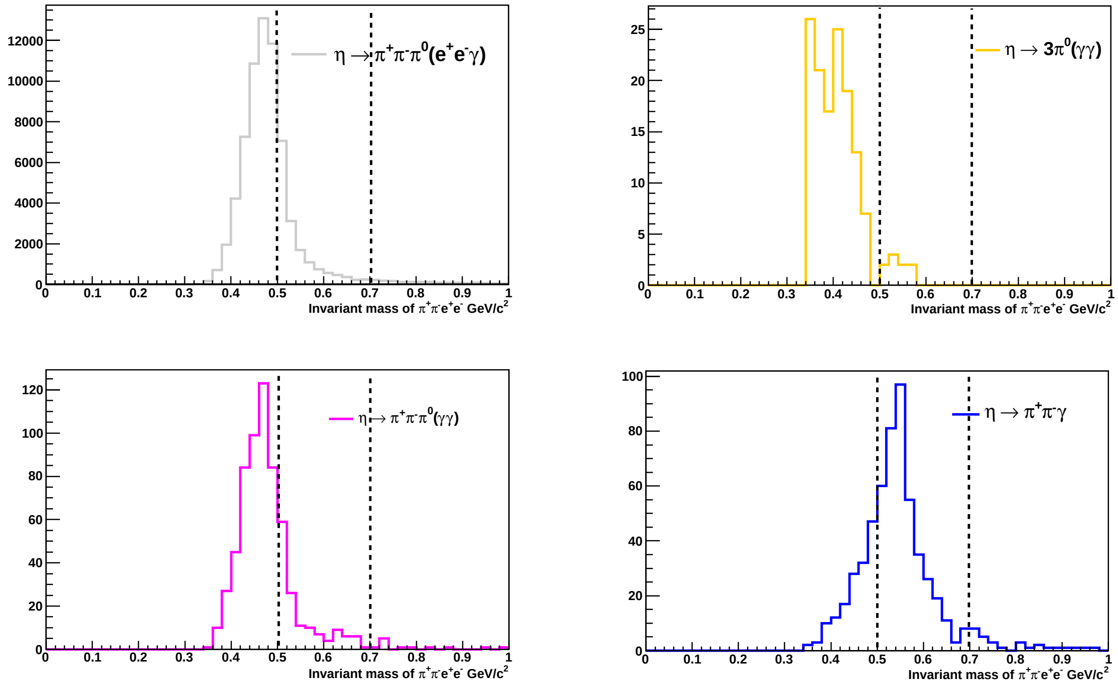

Figure 5.11: Invariant mass distributions simulated for background channels.

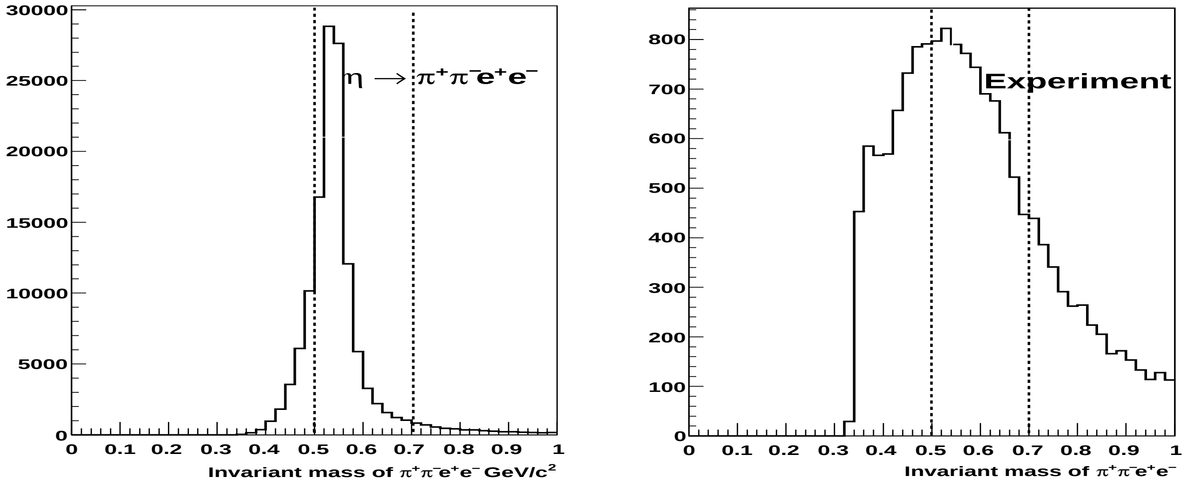

Figure 5.12: (Right panel) – the simulated invariant mass distribution determined for the reaction $pd \rightarrow^3 He\ \eta(\pi^+\pi^-e^+e^-)$. (Left panel) – the experimental invariant mass distribution for events identified as $pd \rightarrow^3 He\eta \rightarrow^3 He\pi^+\pi^-e^+e^-$.

Optimizing the losses of the $\eta \rightarrow \pi^+\pi^-e^+e^-$ decays and reduction of background channels the constraint has been set in the range 0.5–0.7 $\frac{GeV}{c^2}$ as the optimum which reduce significantly the background and keep the 76 % of $\eta(\pi^+\pi^-e^+e^-)$ candidates. The cut is indicated as dashed lines in Fig. 5.11, Fig. 5.12 and Table 5.2 shows cut influence on described reactions.

**Efficiency of the invariant mass cut**

| No. | Reaction | Efficiency [%] | |
|---|---|---|---|
| 2 | $pd \rightarrow^3 He\ \eta \rightarrow^3 He\ \pi^+\pi^-\gamma$ | 66.8 | background |
| 4 | $pd \rightarrow^3 He\ \eta \rightarrow^3 He\ \pi^+\pi^-\pi^0(\gamma\gamma)$ | 22.0 | background |
| 5 | $pd \rightarrow^3 He\ \eta \rightarrow^3 He\ \pi^+\pi^-\pi^0 \rightarrow^3 He\ \pi^+\pi^-e^+e^-\gamma$ | 22.9 | background |
| 6 | $pd \rightarrow^3 He\ \eta \rightarrow^3 He\ 3\pi^0(\gamma\gamma)$ | 6.6 | background |
| * | $pd \rightarrow^3 He\ \pi^+\pi^-e^+e^-$ | 76.2 | signal |

Table 5.2: The efficiency of the cut on the invariant mass of $\pi^+\pi^-e^+e^-$. Numbers in the first column corresponds to these from Table 5.1. Efficiency denotes the percentage of events with invariant mass of reconstructed $\pi^+\pi^-e^+e^-$ system in the range from 0.5 to 0.7 $\frac{GeV}{c^2}$.

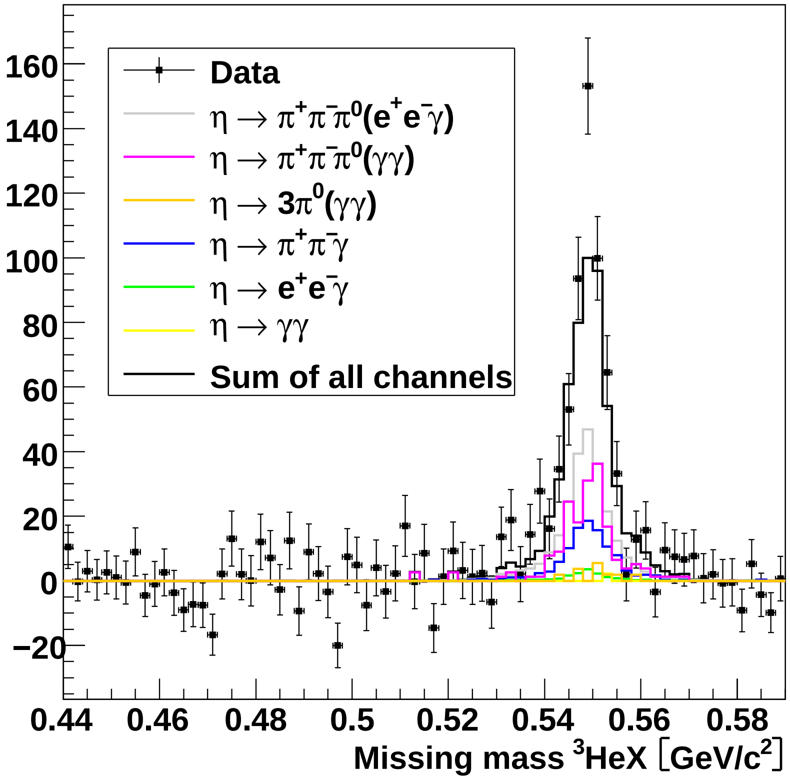

Figure 5.13: The missing mass distribution plotted after the implementation of the invariant mass cut. The lines show total background contribution and also conntributions from decays $\eta \to \pi^+\pi^-\pi^0(e^+e^-\gamma), \eta \to \pi^+\pi^-\pi^0(\gamma\gamma)$, $\eta \to \pi^+\pi^-\gamma$, $\eta \to 3\pi^0$, $\eta \to e^+e^-\gamma$, and $\eta \to \gamma\gamma$.

As can be seen in Fig. 5.13 taking into account the invariant mass of $\pi^+\pi^-e^+e^-$ from the range 0.5 to 0.7 $\frac{GeV}{c^2}$ contributions from channels No. 4, 5, 6 were strongly reduced but the significant contribution originating from reaction No. 2 ($\eta \to e^+e^-\gamma$) was decreased only by the same amount as a signal.

The next step of analysis aims at the further reduction of the largest remaining contribution originating from the $\eta \to \pi^+\pi^-\pi^0(e^+e^-\gamma)$ and $\eta \to \pi^+\pi^-\pi^0(\gamma\gamma)$. The final state of these decays $\pi^+\pi^-e^+e^-\gamma$ differs from the investigated signals by an extra $\gamma$. Unfortunately events with one or more $\gamma$ cannot be cut because also electron and pion from $\eta \to \pi^+\pi^-e^+e^-$ decay often produce in the calorimeter a signal splitted into two clusters where one of these clusters is misidentified with the $\gamma$ (see Fig. 5.14).

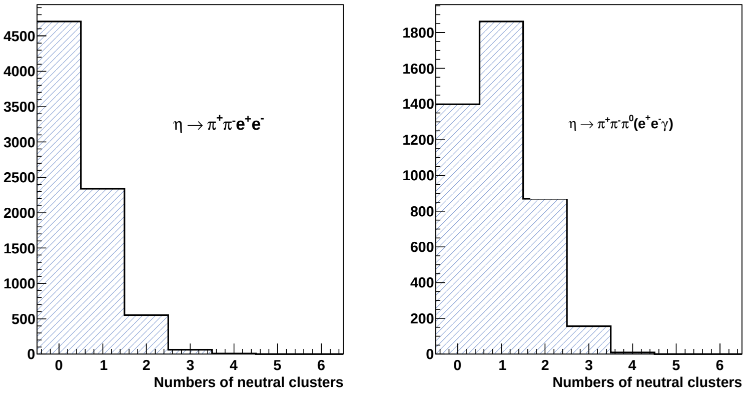

Figure 5.14: Number of reconstructed ”neutral” clusters. (Left panel) – for the $\eta \to \pi^+\pi^-e^+e^-$ reaction, (right panel) – for the $\eta \to \pi^+\pi^-\pi^0(e^+e^-\gamma)$.

In order to distinguish between such spllited signals and real $\gamma$ we take advantage of the fact that distance between clusters in the electromagnetic calorimeter originating from real signals due to $\pi^+\pi^-e^+e^-$ and $\gamma$ from $\pi^0$ decay will on the average larger than the distance between splitted clusters.

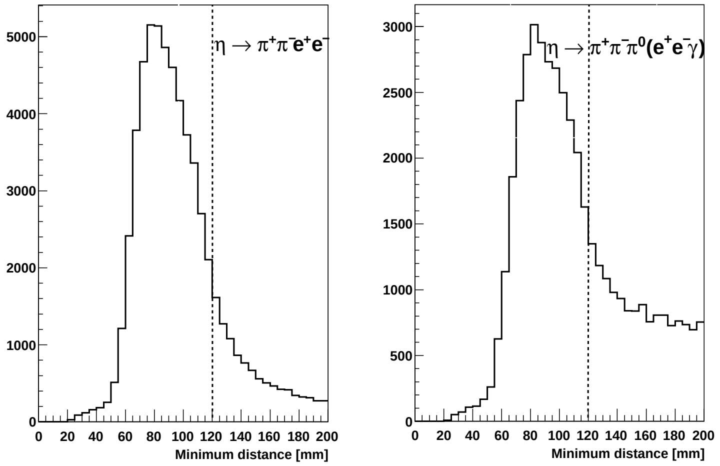

Figure 5.15: The simulated minimum distance distribution. (Left panel) – for the $\eta \to \pi^+\pi^-e^+e^-$ reaction, (right panel) – for the $\eta \to \pi^+\pi^-\pi^0(e^+e^-\gamma)$. The doted line shows the cut applied. Only events with the distance smaller than 12 $cm$ were processed.

Thus as demonstrated in Fig. 5.15 we accept only events having the smallest distance between the cluster associated to the charge track and a neutral cluster smaller than 12 *cm*.
As the extra step the constraint on the smallest opening between charged tracks and the gamma direction has been used instead of the smallest distance criteria. Events which have neutral tracks with the smallest opening angle up to 35° (named later opmin) where processed, Fig. 5.16.

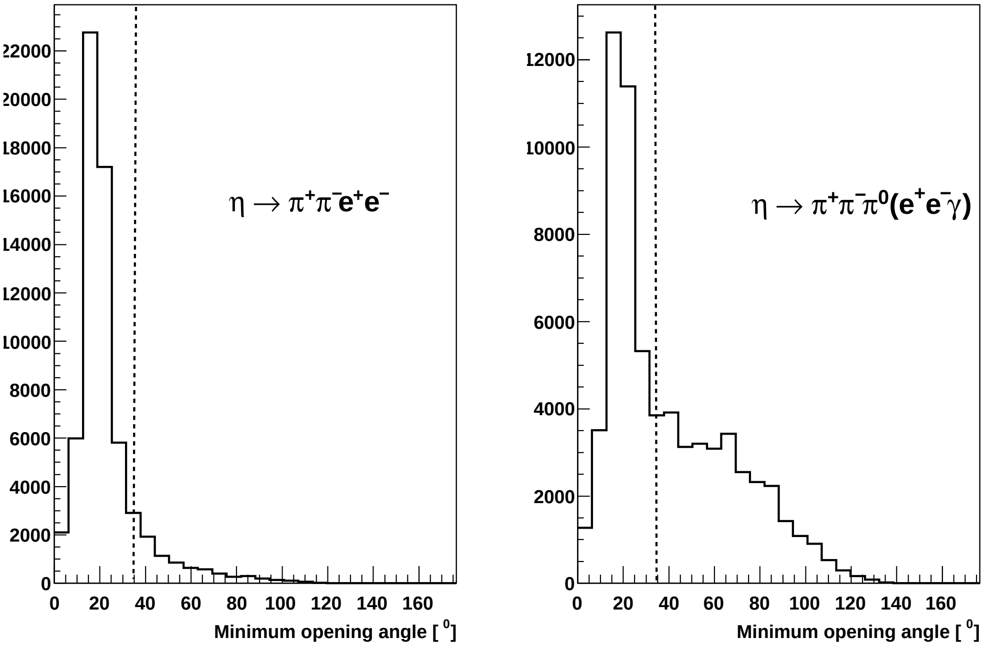

Figure 5.16: The simulated minimum opening angle distribution. (Left panel) – in the $\eta \to \pi^+\pi^-e^+e^-$ reaction, (right panel) – for the $\eta \to \pi^+\pi^-\pi^0(e^+e^-\gamma)$. The doted line demonstrates the cut applied. Events with the minimum opening angle greater than 35° were rejected.

Finally the invariant mass of four charged tracks in the region form 0.5–0.7 $\frac{GeV}{c^2}$ together with minimum distance or minimal opening angle have been set as the final criteria to estimate the number of $\eta \to \pi^+\pi^-e^+e^-$. The efficiency of all used criteria we monitor by simulating missing mass distribution presented in Fig. 5.17.

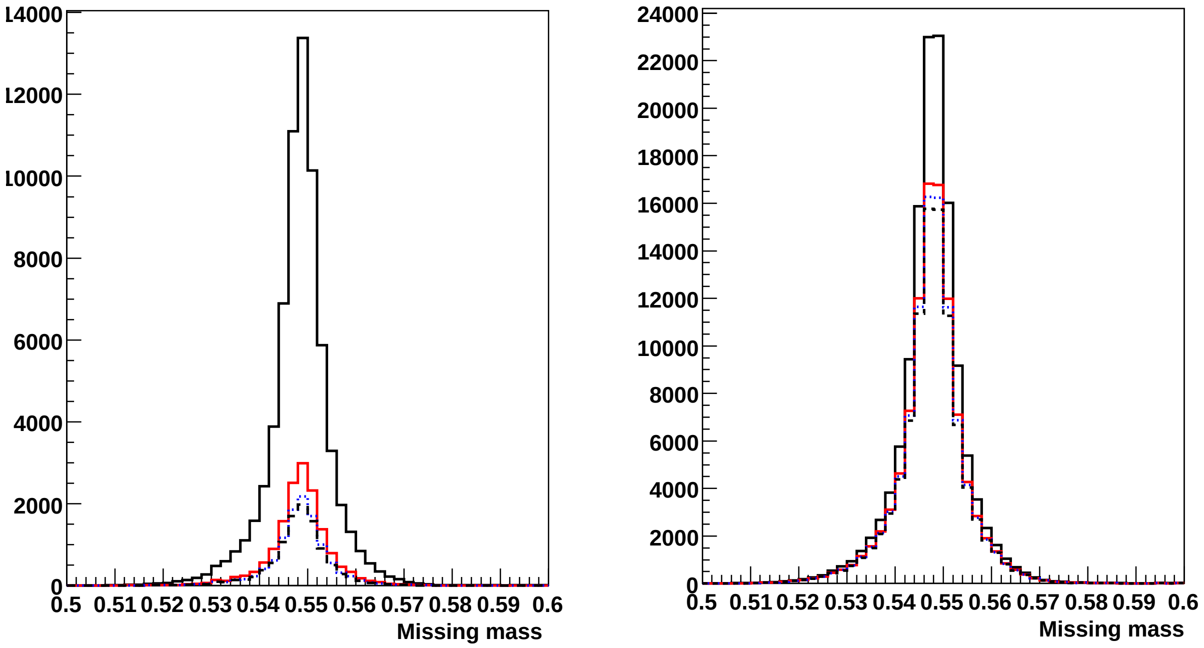

Figure 5.17: The Monte Carlo missing mass distribution. (Right panel) – simulation of the $pd \rightarrow ^3He\ \eta \rightarrow ^3He\ \pi^+\pi^-e^+e^-$. (Left panel) – simulation of the $pd \rightarrow ^3He\ \eta \rightarrow ^3He\ \pi^+\pi^-\pi^0 \rightarrow ^3He\ \pi^+\pi^-e^+e^-\gamma$ process. Full (black) – after identification, Full (red) – invariant mass constraint, Dotted (blue) – IM cut + minimum opening angle less than 35°, Dashed (black) – IM cut + smallest distance less than 120 $mm$.

## 5.3 Branching ratio

All applied limitations shows up the number of candidates for $N_{\eta\rightarrow\pi^+\pi^-e^+e^-}$ which has been established as the integral of the the missing mass distribution after subtraction of the multipion background and simulated background channels from $\eta$ decays (see subsection 5.2.1) presented in Fig. 5.18-5.19:

$$N_{\eta\rightarrow\pi^+\pi^-e^+e^-} = N_{experiment} - N_{multipion} - N_{simulation} \tag{5.4}$$

The statistical error of $N_{\eta\rightarrow\pi^+\pi^-e^+e^-}$ is estimated as $\sqrt{N_{experiment}}$ since the statistical error of the simulation is negligible. In order to evaluate contributions listed in Table 5.1 $2 \times 10^6$ ($N_{generated}$)

events have been generated.

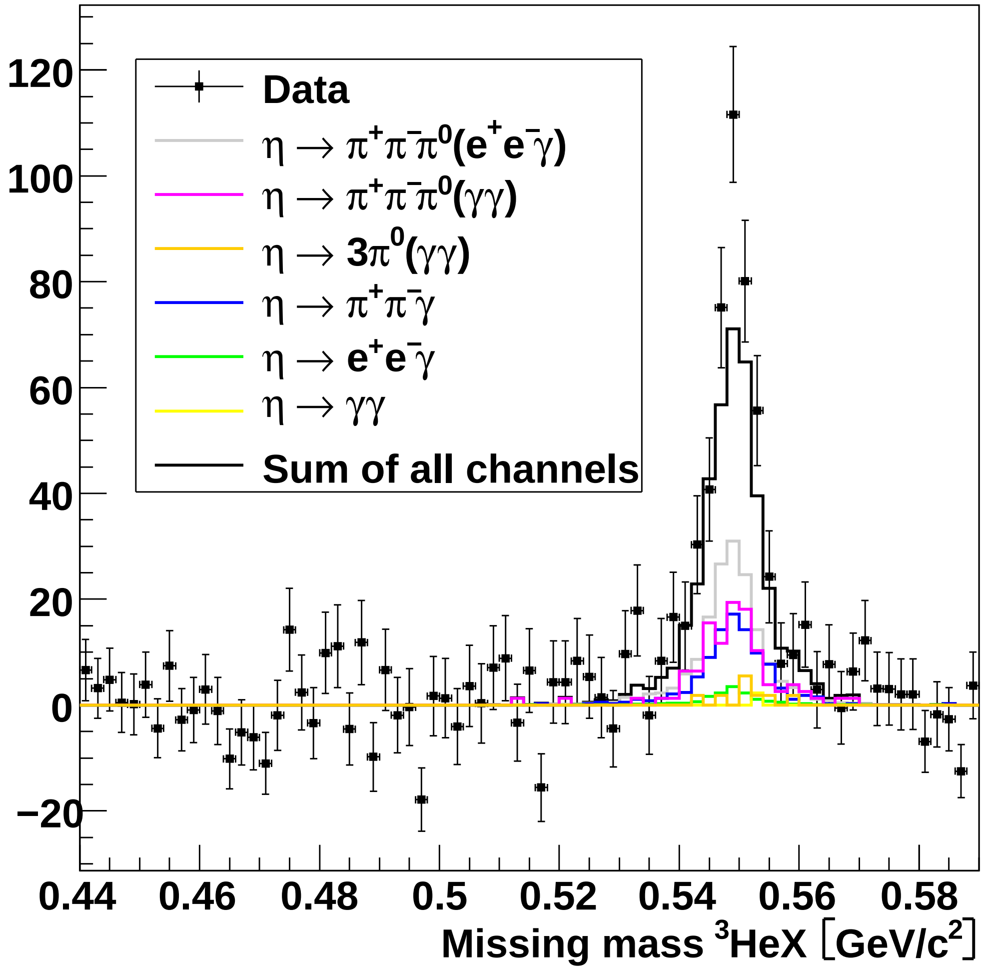

Figure 5.18: Missing mass distribution plotted under condition that invariant mass is in the range from 0.5 - 0.7 $\frac{GeV}{c^2}$ and that the minimum distance between $\pi^+, \pi^-, e^+, e^-$ and gamma candidate is less than 120 $mm$. Contributions from $\eta$ decays are demonstrated in order starting from total background contributions, $\eta \to \pi^+\pi^-\pi^0(e^+e^-\gamma), \eta \to \pi^+\pi^-\pi^0(\gamma\gamma)$, $\eta \to \pi^+\pi^-\gamma$, $\eta \to 3\pi^0$, $\eta \to e^+e^-\gamma$, and ending with $\eta \to \gamma\gamma$.

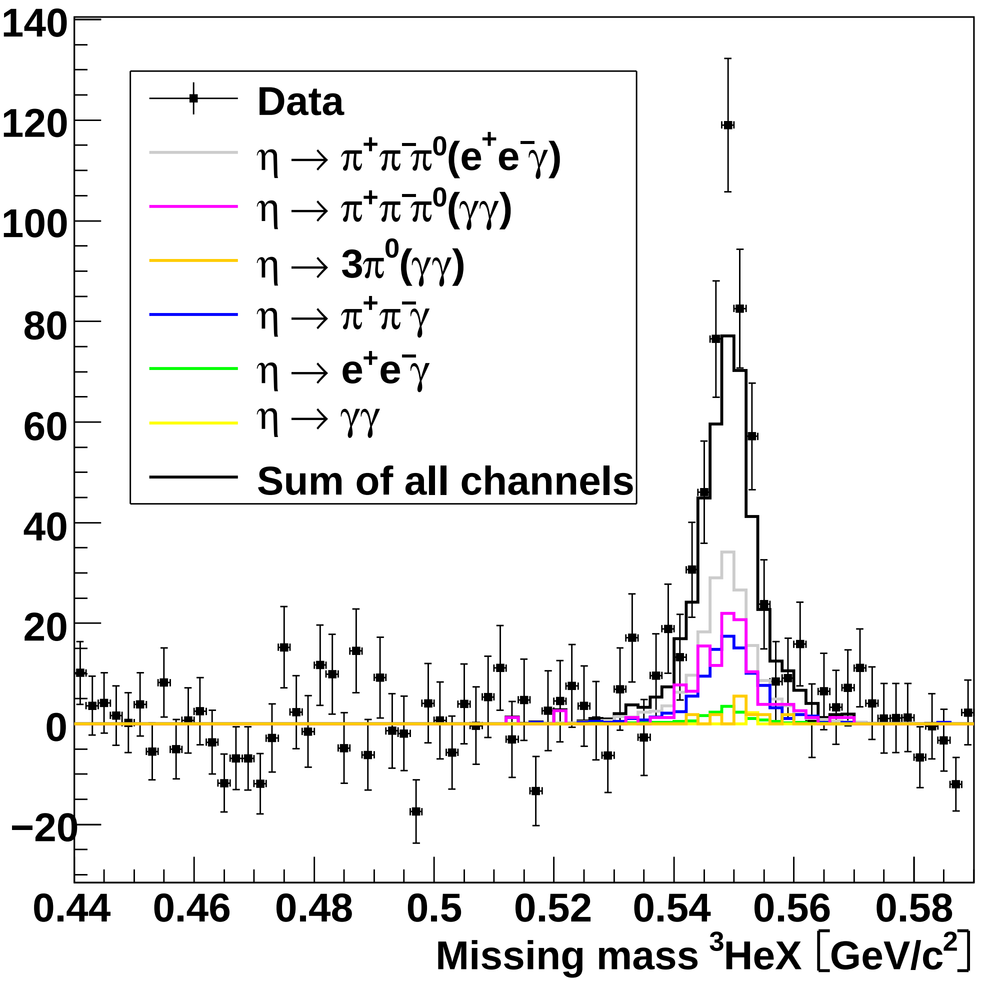

Figure 5.19: Missing mass distribution plotted under condition that invariant mass is in the range from 0.5 - 0.7 $\frac{GeV}{c^2}$and that the minimum opening angle between $\pi^+\pi^-e^+e^-$ and $\gamma$ candidate was lower than 35°. The order of background contributions is same as in the Fig. 5.18.

Taking into account number of $\eta \to \pi^+\pi^-e^+e^-$ events the branching ratios can be evaluated as follows:

$$BR = \frac{N_{\eta\to\pi^+\pi^-e^+e^-} \cdot N_{MC}}{N_\eta^{produced} \cdot N_{\eta\to\pi^+\pi^-e^+e^-}^{MC\ \pi^+\pi^-e^+e^-}} \tag{5.5}$$

where the statistical uncertainty depends predominantly on the error of the $\eta \to \pi^+\pi^-e^+e^-$ events. The BR error was evaluated at each step of the analysis. The results and the number of $\eta \to \pi^+\pi^-e^+e^-$ leftover events after cuts (described in previous subsection) is presented in Table 5.3.

| **Branching ratio** | | | | |
|---|---|---|---|---|
| Method | $N_{\eta\to\pi^+\pi^-e^+e^-}$ | $\Delta N_{\eta\to\pi^+\pi^-e^+e^-}$ | BR | $\Delta BR$ |
| Cut on invariant mass (im cut) | 124 | 35 | $2.65\cdot10^{-4}$ | $0.74\cdot10^{-4}$ |
| im cut + opmin | 131 | 30 | $2.42\cdot10^{-4}$ | $0.61\cdot10^{-4}$ |
| im cut + distance | 139 | 30 | $2.64\cdot10^{-4}$ | $0.69\cdot10^{-4}$ |

Table 5.3: Values of the branching ratio in different analysis steps.

Table 5.3 shows that the results on BR are consistent with each other independent of the cuts applied. As a final results we take:

$$BR = (2.42 \pm 0.61)\cdot 10^{-4} \tag{5.6}$$

since it has the smallest statistical uncertainty.

## 5.4 Systematic uncertainty estimation

The extraction of the $\eta \to \pi^+\pi^-e^+e^-$ events required few crucial assumption and cuts on various variables in the data analysis which could be a source of systematic error to the value of the branching ratio. In this chapter the possible contributions to the systematic uncertainty will be discussed. The value of the systematic uncertainty is calculated as the difference between value of the branching ratio $(2.42\pm0.61_{stat})\cdot10^{-4}$ obtained and the corresponding value obtained after changing of the parameters by their uncertainty in the data analysis and in simulation.

### 5.4.1 Restriction on the time difference between Forward and Central detector

The first criteria applied to the data analysis was the cut on the time difference of particles registered Forward and Central Detector (time cut) (see subsection 5.0.2). In order to estimate the systematic error due to this cut the time range used in the analysis was changed from 22 ns to 30 ns and the full analysis was repeated. Table 5.4 shows the obtained number of events corresponding to $\eta \to \pi^+\pi^-e^+e^-$ and the new BR value and the difference between new value and the results extracted in section 5.3.

| **Branching ratio** | | | | |
|---|---|---|---|---|
| Method | $N_{\eta\to\pi^+\pi^-e^+e^-}$ | $\Delta N_{\eta\to\pi^+\pi^-e^+e^-}$ | BR | $\Delta BR^{sys}_{timecut}$ |
| imcut + opmin | 151 | 32 | 0.000277 | 0.000035 |

Table 5.4: Estimation of the systematic error $\Delta BR^{sys}_{timecut}$ due to the time cut applied in the data analysis.

### 5.4.2 The $^3He$ identification

The identification of the $\eta$ meson production was based on the energy deposition of helium in the Forward Detector. In this analysis a crucial step was a limitation on the sum of energy deposited in the Forward Window Counter (FWC1, FWC2) and the first layer of Forward Trigger Hodoscope (FTH1). To estimate influence of this energy cut on the number of extracted $\eta \to \pi^+\pi^-e^+e^-$ events the limitation was changed from 0.010 to 0.012 $GeV$ and the analysis has been redone. Table 5.5 shows the result.

| **Branching ratio** | | | | |
|---|---|---|---|---|
| Method | $N_{\eta\to\pi^+\pi^-e^+e^-}$ | $\Delta N_{\eta\to\pi^+\pi^-e^+e^-}$ | BR | $\Delta BR^{sys}_{edepcut}$ |
| imcut + opmin | 157 | 32 | 0.000287 | 0.000045 |

Table 5.5: Estimation of the systematic error $\Delta BR^{sys}_{edepcut}$ due to the energy cut applied in the data analysis.

### 5.4.3 The identification of $\pi^+, \pi^-, e^+, e^-$

The identification of pions and leptons is made based on the energy deposited vs. momentum plot described in section 5.1.2. In this step of analysis we draw the function dE–P and identify leptons using graphical region and leftovers were consider as pions. To estimate influence of this criteria the area of this shape has been increased by 10 % and the analysis has been redone. The difference between values of BR obtained in part 5.3 and new results illustrates the systematical uncertainty. Table 5.6 the shows result in the same way as in previous tables.

| **Branching ratio** | | | | |
|---|---|---|---|---|
| Method | $N_{\eta\to\pi^+\pi^-e^+e^-}$ | $\Delta N_{\eta\to\pi^+\pi^-e^+e^-}$ | BR | $\Delta BR^{sys}_{graphcut}$ |
| imcut + opmin | 163 | 31 | 0.000276 | 0.000034 |

Table 5.6: Estimation of the systematic error $\Delta BR^{sys}_{graphcut}$ due to the identification method applied in the data analysis.

### 5.4.4 Restriction on the invariant mass of $\pi^+, \pi^-, e^+, e^-$

The cut on the invariant mass (im cut) of identified $\pi^+$,$\pi^-$,$e^+$,$e^-$ was used to decrease the contribution form other charged eta meson decays. Therefore it is important to know the contribution of this limitation to the total number of $\eta \to \pi^+\pi^-e^+e^-$ obtained in the section 5.3. The Table 5.7 shows the numbers of $\eta \rightarrow \pi^+\pi^-e^+e^-$ events and respective branching ratio when the region of invariant mass of $\pi^+, \pi^-, e^+, e^-$ has been changed from 0.5 – 0.7 to 0.49 – 0.71 $\frac{GeV}{c^2}$.

| **Branching ratio** | | | | |
|---|---|---|---|---|
| Method | $N_{\eta\rightarrow\pi^+\pi^-e^+e^-}$ | $\Delta N_{\eta\rightarrow\pi^+\pi^-e^+e^-}$ | BR | $\Delta BR^{sys}_{imcut}$ |
| imcut + opmin | 149 | 37 | 0.000246 | 0.000004 |

Table 5.7: Estimation of the systematic error $\Delta BR^{sys}_{imcut}$ due to the invariant mass cut applied in the data analysis.

### 5.4.5 Constraint on the minimum angle between neutral cluster and clusters from $e^+, e^-, \pi^+, \pi^-$

Similar, in oreder to estimate an influence on the result from the restriction on the minimum opening angle (opmin cut) between neutral tracks and $e^+, e^-, \pi^+, \pi^-$ (see part 5.2.2) we change this value from 35 to 37 degrees and calculate to branching ratio accoording to the re–extracted number of $\eta \rightarrow \pi^+\pi^-e^+e^-$ events. Table 5.8 shows the numbers of eta and respective branching ratio calculated using 37 degrees cut.

| **Branching ratio** | | | | |
|---|---|---|---|---|
| Method | $N_{\eta\rightarrow\pi^+\pi^-e^+e^-}$ | $\Delta N_{\eta\rightarrow\pi^+\pi^-e^+e^-}$ | BR | $\Delta BR^{sys}_{opmincut}$ |
| imcut + distance | 148 | 33 | 0.000269 | 0.000027 |

Table 5.8: Estimation of the systematic error $\Delta BR^{sys}_{opmincut}$ due to the minimum opening angle cut applied in the data analysis.

### 5.4.6 Shape of multipion background

The polynomial of the third order and Gauss functions were used as the input to fit procedure to fix the multipion background (bckshape). In oreder to chcek how the change of polynomial changes the branching ratio, the polynomial of 4th order was used and the new BR was obtained. In order to extract systematic uncertainty $\Delta BR^{sys}_{bckshape}$ the difference between newly calculated value and this given in 5.3 has been evaluated and it is given in Table 5.9

| **Branching ratio** | | | | |
|---|---|---|---|---|
| Method | $N_{\eta\to\pi^+\pi^-e^+e^-}$ | $\Delta N_{\eta\to\pi^+\pi^-e^+e^-}$ | BR | $\Delta BR^{sys}_{bckshape}$ |
| imcut + distance | 132 | 30 | 0.000241 | 0.000001 |

Table 5.9: Estimation of the systematic error $\Delta BR^{sys}_{bckshape}$ due to the estimation of the shape of continuous background.

### 5.4.7 Error due to uncertainty of the values of branching ratios

The extracted number of $\eta \to \pi^+\pi^-e^+e^-$ events depends on the values of branching ratio listed in Table 5.10. For the conservative estimation of the influence of these error on the final result the values of background branching ratio have been decreased by their errors and the number of $\eta \to \pi^+\pi^-e^+e^-$ were reevaluated.

| **Branching ratio** | | | | |
|---|---|---|---|---|
| Method | $N_{\eta\to\pi^+\pi^-e^+e^-}$ | $\Delta N_{\eta\to\pi^+\pi^-e^+e^-}$ | BR | $\Delta BR^{sys}_{brmaxcut}$ |
| imcut + distance | 142 | 31 | 0.000261 | 0.000019 |

Table 5.10: Estimation of the systematic error $\Delta BR^{sys}_{brmax}$ due to the uncertainty of the branching ratios of background decays.

### 5.4.8 Evaluation of the number of $\eta$ registered

The number of $\eta$ mesons produced in $pd \to^3 He\eta$ reaction has been determined using fit procedure discussed in 5.1. In order to obtain the systematical uncertainty we change to polynomial component from 3rd to the 4th degree which results in number of eta mesons 10828000. The difference between 10816000 estimated in the nominal analysis is negligible in view of other errors.

### 5.4.9 Spatial resolution of the Mini Drift Chamber

In the nominal analysis we used drift chamber resolution of 325 $\mu$m as discussed in part 4.4, for the determination of systematics we reanalyzed the data with $\sigma = 500\ \mu m$ and found negligible change in the number of reconstructed $\eta \to \pi^+\pi^-e^+e^-$.

### 5.4.10 Total systematical uncertainty

Taking into account nine above discussed independent contributions to the systematic error we determined the total systematic uncertainty to $0.75 \cdot 10^{-4}$ adding all contribution in quadrature. Thus the final result on the BR ratio for $\eta \to \pi^+\pi^-e^+e^-$ extracted in this thesis reads:

$$BR = (2.42 \pm 0.61_{stat.} \pm 0.74_{sys.}) \cdot 10^{-4} \tag{5.7}$$

## 5.5 Distribution of dihedral angle

As it was presented in chapter 2 the decay rate $\eta \to \pi^+\pi^-e^+e^-$ allows to study the level of CP conservation via distribution of the dihedral angle between $\pi^+\pi^-$ and $e^+e^-$ emission planes. First we calculate the dihedral angle ($\phi$) (see subsection 2.3) in the rest frame of the $\eta$ meson using the four momentum vectors of $\pi^+, \pi^-, e^+, e^-$ of candidates to $\eta \to \pi^+\pi^-e^+e^-$. Next we calculated the missing mass in respect to $\phi$ from 0 to 90 and 90 to 180 degrees. Finally, using the procedure of background determination we calculated the number of $\eta$ meson decaying into $\pi^+\pi^-e^+e^-$ for both angular ranges separately. Table 5.11 shows results.

| $\phi$ range | $N_{\eta\to\pi^+\pi^-e^+e^-}$ | $\Delta N_{\eta\to\pi^+\pi^-e^+e^-}$ |
|---|---|---|
| $0° - 90°$ | 80 | 23 |
| $90° - 180°$ | 72 | 21 |

Table 5.11: Numbers of $\eta \to \pi^+\pi^-e^+e^-$ extracted for two ranges of angle $\phi$.

The asymmetry derived from the numbers shown in Table 5.11 is equal to:

$$A = (5 \pm 20) \cdot 10^{-2} \tag{5.8}$$

# Chapter 6

# Conclusion

The main results of this thesis is the estimation of the branching ratio for the $\eta \rightarrow \pi^+\pi^-e^+e^-$ reaction. The statistics has been increased by almost an order of magnitude with respect to the sample of $\eta \rightarrow \pi^+\pi^-e^+e^-$ available before present measurement [10, 8]. Based on $131 \pm 30$ decay events we determined the value of branching ratio to be $(2.42 \pm 0.61_{stat.} \pm 0.74_{sys.}) \cdot 10^{-4}$ which is consistent with the results obtained meantime by KLOE collaboration [54] ($(2.68 \pm 0.09_{stat.} \pm 0.07_{sys.}) \cdot 10^{-4}$). Moreover, we have established that the distribution of dihedral angle distribution of $\pi^+\pi^-$ and $e^+e^-$ planes indicates no assymetry on the level of 20 %. This result is also consistent with the assymetry determined recently by the KLOE collaboration [54] ($A_\phi = (-0.6 \pm 2.5_{stat.} \pm 1.8_{sys.}) \cdot 10^{-2}$).
The data evaluated originate from the measurement performed in November 2008. The $\eta$ meson has been produced via $pd \rightarrow ^3He\eta$ reaction using the COSY proton beam and the deuteron pellet target of the WASA detector. The kinetic energy of $^3He$ was determined based on its energy loss in the scintillators planes placed in the forward part of the WASA–at–COSY detector facility. The momentum direction of $^3He$ has been determined from direction of its trajectory reconstructed using signals in drift chambers built out of gaseous straws proportional counters. The identification of the $\eta$ mesons has been realized using conservation of the energy and momentum via calculation of the missing mass. The decay products have been measured in the central part of the WASA–at–COSY detector. Momentum vectors of the leptons and $\pi^+$ and $\pi^-$ have been determined using the track curvature reconstructed from signals in seventeen cylindrical planes of mylar straw detectors. The straw chamber has been placed inside the Superconducting Solenoid delivering magnetic field parallel to the COSY ion beam. The identification of pions and leptons was done by the energy loss in a plastic scintillator barrel and an electromagnetic calorimeter surrounding the straw chamber.

This work allowed to reconstruct more than hundred of $\eta \rightarrow \pi^+\pi^-e^+e^-$ events based on the sample of the $10^7$ $\eta$ mesons. Meantime the WASA–at–COSY group collected in the year 2009 and 2010 about $3 \cdot 10^7$ $\eta$ mesons using $pd \rightarrow ^3He\eta$ rection and more than $10^8$ data sample have been achieved in $pp \rightarrow pp\eta$ process.

The data will be collected further in the years 2011–2014. This will significantly improve the statistics. This new data will be analyzed in the near future. The WASA–at–COSY has a long term physics program where charged decays can be measured till 2014 year and will further increase significantly the statistics also for $\eta \rightarrow \pi^+\pi^-e^+e^-$ reaction.

# Chapter 7

# Acknowledgments

Firstly I would like to express my gratitude to Prof. UJ, Dr. hab Pawel Moskal for his patience and bringing ideas and help.
I am extremely grateful to Dr. Magnus Wolke for possibility to participate in physics program of the WASA–at–COSY collaboration, the invitation to the Research Centre Jülich, and for his help concerning physics motivation for the measurement of the $\eta \to \pi^+\pi^-e^+e^-$. I would like to acknowledge Prof. Hans Stroeher and Prof. Jim Ritman for the opportunity to work in the Research Centre Jülich.
I am grateful to Prof. Boguslaw Kamys for possibility to prepare this dissertation in the Faculty of Physics, Astronomy and Applied Computer Science of the Jagellonian University.

I am grateful to Dr. Henner Ohm, Dr. Valerji Serdyuk, Dr. Paweł Kulessa and Dr. Krzysztof Pysz for their transfer of knowledge dedicated to gaseous detectors and collaboration during installation of the Forward Proportional Chamber.
Special acknowledgments are due to Dr. Andrzej Kupść for providing me all information about WASA detector and the software used during analysis and to Prof. Joanna Stepaniak for her valuable help and advices in the data analysis.
I want to say special thanks to Dr. Volker Hejny for his enormous help and patience during creation of the analysis software.
I am grateful to Dr. Christoph Redmer, Marcin Berłowski, Leonid Yurev and other people involved in the analysis of charged $\eta$ meson decays in WASA–at–COSY group. Many thanks for reading and correcting the manuscript of this work are due to my supervisor Prof. UJ, Dr. hab Pawel Moskal, Dr. Andrzej Kupść and Prof. Dr. Jerzy Smyrski.

# Appendix A

# Detector sensitivity for the form factor determination

The decay can also provide information about the transition Form Factor (FF), which can be extracted from the distribution of the dilepton invariant mass ($q$). Due to lack of the statistics the point has not been the subject of this thesis. Despite the fact, we want to emphasize the statistical requirements to the determination of FF.

The FF is usually parametrized by a single pole formula: $FF(q^2) = \Lambda^2/(\Lambda^2 - q^2)$. For the decay $\eta \rightarrow \pi^+\pi^-e^+e^-$ the $q$ value is restricted to the range $4m_e < q < m_\eta - 2m_\pi$. The statistical uncertainty of the $\Lambda$ was extracted from Monte Carlo data samples of $\eta \rightarrow \pi^+\pi^-e^+e^-$ decays generated with the $\Lambda$ set to 0.77 GeV. The accuracy of the $\Lambda$ can be parametrized as follows:

$$\Delta\Lambda = C\frac{\sqrt{N_S + N_B}}{N_S}. \tag{A.1}$$

where $C \approx 20$ GeV, $N_S$, $N_B$ are the number of signal and background events respectively. In order to get e.g. $\Delta\Lambda = 0.1$ GeV a data sample of more than $10^5$ collected events is required [55].

# List of Figures

# Bibliography

[1] A. Alavi-Harati et al. Observation of CP violation in $K_L \to \pi^+\pi^-e^+e^-$ decays. *Phys. Rev. Lett.*, 84:408–411, 2000.

[2] A. Lai et al. Investigation of $K_{L,S} \to \pi^+\pi^-e^+e^-$ decays. *Eur. Phys. J.*, C 30:33–49, 2003.

[3] K. Abe et al. Measurement of the branching fraction for $B \to \eta' K$ and search for $B \to \eta'\pi^+$. *Phys. Lett.*, B 517:309–318, 2001.

[4] Bernard Aubert et al. Measurement of CP violating asymmetries in $B^0$ decays to CP eigenstates. *Phys. Rev. Lett.*, 86:2515–2522, 2001.

[5] B. H. Behrens et al. Two–body $B$ Meson Decays to $\eta$ and $\eta'$: Observation of $B \to \eta' K$. *Phys. Rev. Lett.*, 80:3710–3714, 1998.

[6] T. E. Browder et al. Observation of High Momentum $\eta'$ Production in $B$ Decays. *Phys. Rev. Lett.*, 81:1786–1790, 1998.

[7] S. J. Richichi et al. Two–body $B$ Meson Decays to $\eta$ and $\eta'$: Observation of $B \to \eta K^*$. *Phys. Rev. Lett.*, 85:520–524, 2000.

[8] Chr. Bargholtz et al. Measurement of the $\eta \to \pi^+\pi^-e^+e^-$ decay branching ratio. B644:299–303, 2007.

[9] M. Berlowski et al. Measurement of eta meson decays into lepton-antilepton pairs. *Phys. Rev.*, D77:032004, 2008.

[10] R. R. Akhmetshin et al. Study of conversion decays $\phi \to \eta e^+e^-$, $\eta \to e^+e^-\gamma$ and $\eta \to \pi^+\pi^-e^+e^-$ at CMD–2. *Phys. Lett.*, B501:191–199, 2001.

[11] M. Jacewicz and Bo Hoistad. Proceedings of the Second International Workshop on Eta Meson Physics. 2007.

[12] C. Amsler and others (Particle Data Group). 1 (2008) and 2009 partial update for the 2010 edition. *Phys. Lett.*, B 667, 2008.

[13] A. Pais and Trieman. S. B. 168:1858, 1968.

[14] L. M. Sehgal and M. Wanninger. CP violation in the decay $K_L \to \pi^+\pi^-e^+e^-$. *Phys. Rev.*, D46:1035–1041, 1992.

[15] A. Glossanov. Measurements of CP violation and $K_0$ Charge Radius using $K_L \to \pi^+\pi^-e^+e^-$ decays. PhD thesis, may 2005.

[16] Dao-Neng Gao. The CP–violating asymmetry in $\eta \to \pi^+\pi^-e^+e^-$. *Mod. Phys. Lett.*, A 17:1583–1588, 2002.

[17] D. E. Groom et al. Review of particle physics. *Eur. Phys. J.*, C15:1–878, 2000.

[18] J. Wess and B. Zumino. Consequences of anomalous ward identities. *Phys. Lett.*, B 37:95–97, 1971.

[19] E. Witten. Global aspects of current algebra. *Nucl. Phys.*, B 223:422–432, 1983.

[20] B. Borasoy and R. Nissler. Hadronic decays of $\eta$ and $\eta'$. *AIP Conf. Proc.*, 796:150–153, 2005.

[21] B. Borasoy and R. Nissler. $\eta, \eta' \to \pi^+\pi^-l^+l^-$ in a chiral unitary approach. 0500.

[22] L. G. Landsberg. Electromagnetic decays of light mesons. *Phys. Rept.*, 128:301–376, 1985.

[23] C. Jarlskog and H. Pilkuhn. Eta decays with $e^+e^-$ and $\mu^+\mu^-$ pairs. *Nucl. Phys.*, B 1:264–268, 1967.

[24] J. Stepaniak et al. Dilepton pair production: Phenomenology and experiment. *Phys. Scripta*, T99:133–139, 2002.

[25] L. Ametller, L. Bergström, A. Bramon, and E. Masso. The quark triangle: Application to pion and eta decays. *Nucl. Phys.*, B 228:301–315, 1983.

[26] L. Ametller. $\eta$ decays Involving Photons. *Phys. Scripta*, T 99:45–54, 2002.

[27] K. Schonning et al. The $pd \rightarrow^3 He\eta \rightarrow \pi^0$ reaction at $T_p = 1450$ MeV. *Phys. Lett.*, B685:33–37, 2010.

[28] K. Schoenning et al. Production of eta and $3\pi$ mesons in the $pd \rightarrow^3 HeX$ reaction at 1360 and 1450 MeV. 2010.

[29] R. Maier. Cooler synchrotron COSY: Performance and perspectives. *Nuclear Instrument and Methods*, A390:1–8, 1997.

[30] http://www.fz-juelich.de/ikp/anke/de/index.shtml.

[31] http://www.fz-juelich.de/ikp/COSY-TOF/index.html.

[32] H. H. Adam et al. Proposal for the Wide Angle Shower Apparatus (WASA) at COSY-Juelich - WASA at COSY. 2004.

[33] http://www.iskp.uni-bonn.de/gruppen/edda/index.html.

[34] A. Budzanowski et al. IKP/COSY Annual Report, Jul-374, 1999.

[35] Brauskiepe S. et al. *Nucl. Instr. Meth.*, A376:397–410, 1996.

[36] K. Nuenighoff et al. Investigations of the neutron performance of a methane hydrate moderator. *nim*, 562(2):565 – 568, 2006.

[37] D. Grzonka and K. Kilian. Experiments at COSY. *Nucl. Phys. A*, 670(1-4):241 – 248, 2000.

[38] D. Prasuhn et al. Electron and stochastic cooling at COSY. *Nuclear Instrument and Methods*, A441:167–174, 2000.

[39] Chr. Bargholtz et al. The wasa Detector Facility at CELSIUS. *Nucl. Instrum. Meth.*, A594:339–350, 2008.

[40] C. Adolph et al. Measurement of the $\eta \rightarrow^3 \pi^0$ Dalitz Plot Distribution with the WASA Detector at COSY. *Phys. Lett.*, B677:24–29, 2009.

[41] C. F. Redmer. In search of the Box-Anomaly with the WASA facility at COSY. PhD thesis, 2010.

[42] P. Vlasov. Analysis of the $\eta \rightarrow 3\pi^0$ decay in the pp interaction. PhD thesis, dec 2008.

[43] R. J. M. Y. Ruber, M. Blom, H. Caln, C. J. Fridn, A. Larsson, G. Norman, A. Yamamoto, H. Yamaoka, Y. Makida, N. Kimura, K. Tanaka, M. Iida, H. Ohhata, H. Hirabayashi, N. Takasu, and A. Nawrot. *Nucl. Instrum. Meth.*, A 503(3):431 – 444, 2003.

[44] M. Jacewicz. Measurement of the reaction $pp \rightarrow \pi^+\pi^-\pi^0$ CELSIUS/WASA at 1.36 GeV. PhD thesis, dec 2005.

[45] H. Kleines et al. The new DAQ system for WASA at COSY. *IEEE Trans. Nucl. Sci.*, 53:893–897, 2006.

[46] V. Hejny et al. Performance issues of the new DAQ system for WASA at cosy. *IEEE Trans. Nucl. Sci.*, 55:261–264, 2008.

[47] P. Marciniewski. Fast Digital Trigger Systems for Experiments in High Energy Physics. PhD thesis, 2001.

[48] K. Fransson. The trigger system of the CELSIUS/WASA detector. *Phys. Scripta*, T99:176–182, 2002.

[49] G Charpak et al. Some read-out systems for proportional multiwire chambers. *Nucl. Instrum. Meth.*, 65:217–220, 1968.

[50] G. Charpak. Development of multiwire proportional chambers. *CERN Cour.*, 6:174–176, 1969.

[51] G. Charpak. Particle detection by gas discharges. (in french). *J. Phys. (France)*, 30:C2–C86, 1969.

[52] G. Charpak. High-accuracy position measurements with drift chambers and proportional chambers (talk). *IEEE Trans. Nucl. Sci.*, 21:38–44, 1974.

[53] J. Złomańczuk. Uppsala Universty, Priv Com., 2009.

[54] F. Ambrosino et al. Measurement of the branching ratio and search for a cp violating asymmetry in the $\eta \rightarrow \pi^+\pi^-e^+e^-(\gamma)$ decay at KLOE. 2008.

[55] Janusz M. and Kupsc A. IKP/COSY Annual Report, Jul-4242, 2007.